Development of Electrochemical Processes for More Practical and Effective Onsite Wastewater Treatment

Thesis by

Seungkyeum Kim

In Partial Fulfillment of the Requirements for
the Degree of
Doctor of Philosophy

Caltech

CALIFORNIA INSTITUTE OF TECHNOLOGY
Pasadena, California

2022
(Defended May 23, 2022)

Seungkyeum Kim
ORCID: 0000-0002-0948-6452

ACKNOWLEDGEMENTS

What a journey! I would not have been able to finish this 5-year journey without all the help and support from people around me. First, I would like to thank my Ph.D. advisor, Mike. Throughout all my years at Caltech, I have not been quite certain about what I wanted to pursue after graduation. Thanks to Mike's willingness to allow me to explore my interests outside research, I was able to gain some valuable experiences in industry and different research area. He has been always very supportive of my decisions, which I can't thank enough.

I also thank all the group members who have been always willing to provide help for me. My life at Caltech has been much more enjoyable thanks to them. When I first joined the group, I learned and grew a lot as a creative researcher by working with Cody. And, having a buddy like Axl alongside made it more fun to run experiments that could have been more tiresome otherwise. Jonghun and Yang helped me to devise and execute my first independent research project. I would have been very lost without their assistance and supervision. It was not until I worked with Clement that I grasped a great amount of knowledge about wastewater treatment technologies. It was such a rewarding experience to work with him and Leo and get to publish our work during the pandemic. I have formed close friendships with Alan, Sam, Jing, and Yan. I am very grateful to have precious memories both in and outside lab with them. Also, it has been always pleasurable to chat with Heng, Sean, and Lei. Outside the Hoffmann group, I appreciate the companionship and friendship with Hyeongjoo and Jin. We suffered together; we laughed together; and, we had fun together.

During my internship at Lam Research, Nemo, Patrick, and Shirley were such great mentors to guide and supervise someone like myself without any industrial experience. And, thanks to DJ, Yoojung, and Kevin, my life in the bay area was filled with joy and fun. I am thankful to have built closer friendships with them. Also, I appreciate the guidance, supervision, and assistance from Dr. Marcus Baer, Dr. Johannes Frisch, and Tsung-En during my research internship at Helmholtz Zentrum Berlin.

I can't imagine what my graduate school life would have been without my friends: Emily, Jennifer, Harry, Hunjoo, Haesol, Anthony, Felicia, and Jason. They have been always there to listen and cheer me up whenever I need. However far they were from me, their support and kindness eased my anxiety and concerns. Especially, Emily always lifted my spirits with her liveliness; Jennifer and Harry always cared for me and made me feel special; and Hunjoo was always all ears to my problems no matter how trivial they were. And I couldn't be more grateful for them to accept me for who I am. I wish I had known earlier that I was in the good old days with my friends before I actually left them. But I will never forget those wonderful memories we have.

마지막으로 한국에 있는 우리 가족들과 친구들. 5 년이라는 짧지 않은 시간이 어떻게 지나갔는지 모르겠습니다. 처음엔 죽기 살기로 버틸려고 했고 어느 정도 익숙해지니 어디로 가야할지 길을 잃고 헤매기도 했지만 덕분에 여기까지 왔습니다. 연구 자체도 힘들 때가 있었지만 지난 대학원 생활을 돌이켜보면 개인적인 일들로 더 힘든 시간들을 보낸거 같습니다. 그럴 때마다 한국에 있는 가족들과 친구들 덕분에 힘이 나고 이겨낼 수 있었습니다. 박사 1 년차 처음하는 연애로 방황할 때 항상 내 얘기를 들어주고 이해해 주었던 누나, 박사 3 년차 저를 있는 그대로 받아주신 부모님, 박사 4 년차 첫 이별로 마음 아팠을 때 항상 옆에 있어 주었던 우리 가족들 감사하고 사랑합니다. 그리고 멀리 한국에서도 항상 힘과 말벗이 되어 준 친구들 진규, 민지, 수정, 그리고 연오. 그리고 지금은 미국에 있는 영재형. 어렸을 때부터 지금까지 이어온 소중한 인연들에 감사합니다.

ABSTRACT

In spite of the lack of safely managed sanitation and water supply systems, developing countries with rapid urbanization cannot afford to implement advanced treatment technologies that are highly centralized, calling for the development of practical onsite wastewater treatment. As effective yet practical solutions to the water crisis, I have developed high-performance earth-abundant electrocatalysts and an uncoupled electro-peroxone (E-peroxone) prototype reactor that can be applied in and as decentralized wastewater treatment systems. A series of conductive TiO_2 nanotube array electrodes are known to be effective for chlorine evolution reaction (CER) for wastewater treatment and oxygen evolution reaction (OER) for water splitting. In order to further enhance their electrocatalytic activities, an ultrathin layer of Al_2O_3 was deposited onto TiO_2 nanotube arrays via atomic layer deposition (ALD). Due to the facilitated formation of Ti^{3+} and oxygen vacancies by Al_2O_3 ALD, black TiO_2 nanotube arrays with 8 ALD cycles achieved up to 30% enhancement in CER and OER overpotentials in comparison to those without Al_2O_3 coating. Moreover, the ultrathin Al_2O_3 overlayer (~2 nm) reduced the charge transfer resistance and increased the electrochemical chemical surface area (ECSA) 3-fold for both reactions. Black TiO2 nanotube arrays with 8 cycles were applied for toilet wastewater treatment and outperformed a dimensionally stable anode (DSA) in terms of chemical oxygen demand (COD) and ammonia reductions. The simplicity of the synthetic procedures and the use of inexpensive metal oxides suggest that Al_2O_3-deposited TiO_2 nanotube arrays can provide a promising approach to wastewater treatment and water splitting as practical alternatives for costly DSAs.

The uncoupled E-peroxone reactor system integrates ozonation with in situ hydrogen peroxide (H_2O_2) production to generate hydroxyl radicals for wastewater treatment. The E-peroxone process variables such as H_2O_2 concentration and ozone dose were optimized to maximize the treatment efficiency. Consequently, the system succeeded in reducing COD by 89%, total organic carbon (TOC) by 91%, biochemical oxygen demand (BOD) by 86%, and turbidity by 95% after 90-minute treatment of synthetic graywater. Moreover, the system reclaimed treated wastewater as an electrolyte for H_2O_2 production for subsequent treatment and maintained over 80% and 70% reductions in COD and TOC, respectively, over four consecutive treatment cycles. This system does not need any chemical additive, utilizes the energy-efficient E-peroxone process, and comprises inexpensive, accessible components. As a result, these advantages significantly reduce the system’s capital and operational costs. The promising results and cost-effectiveness show that it can provide a viable solution for the treatment of graywater and human wastewater in low-resource settings.

PUBLISHED CONTENT AND CONTRIBUTIONS

Chapter 3 was reprinted with permission from:

Dobelle, L.; Kim, S.; LeVan, A. X.; Leandri, H.; Hoffmann, M. R.; Cid, C. A. Onsite Graywater Treatment in a Two-Stage Electro-Peroxone Reactor with a Partial Recycle of Treated Effluent. *ACS EST Eng.* **2021**, *1* (12), 1659–1667. https://doi.org/10.1021/acsestengg.1c00240.

> L.D. and S.K. contributed equally to the work. L.D., S.K., A.L., and H.L. carried out the experiments. L.D. and S.K. co-wrote the manuscript with support from A.L., C.C., and M.H. C.C. conceived the original idea and helped supervise the project. M.H. supervised the project.

TABLE OF CONTENTS

LIST OF FIGURES AND TABLES

Chapter 2

Chapter 3

NOMENCLATURE

Chlorine Evolution Reaction (CER). The chemical production of reactive chlorine species (i.e., Cl_2, HOCl, and OCl^-).

Dimensionally Stable Anode (DSA). Anodes with high electrical conductivity and corrosion resistance for electrochemical applications.

Graywater. Domestic or commercial wastewater that has not been in contact with streams with fecal contamination.

Oxygen Evolution Reaction (OER). The chemical production of oxygen gas (i.e., O_2).

CHAPTER 1: Introduction

1.1. Problem Statement

More than 1 billion people in developing countries are estimated to be in dire need of safely managed sanitation services and water supply systems.[1] They are exposed to a number of life-threatening waterborne pathogens as a result of open defecation and direct human waste release without proper treatment. Not only do the poor sanitation systems put billions of people's health at a serious risk, but they also pose a threat to biodiversity by disturbing the aquatic ecosystems with untreated human waste. Unfortunately, advanced treatment technologies that are highly centralized require infrastructure beyond the financial and systematic capabilities of developing countries. This complication calls for novel practical paradigms for sanitation and water supply, namely decentralization in wastewater treatment management.[2]

There has been a lot of research focusing on the innovation of wastewater treatment and reuse applications with enhanced water quality and productivity for non-potable practices. Considering the financial and technological restrictions present in the developing world, the new wastewater treatment and reuse systems are required to be available for onsite use and practical in terms of energy and material costs. Tackling today's wastewater treatment challenges of energy efficiency and environmental footprint, our research group has been designing electrolysis cells and electrochemical reactors for decentralized wastewater management integrated with water recycling and reuse systems.

As part of my Ph.D. thesis, I have developed high-performance earth-abundant electrocatalysts that could replace conventional dimensionally stable anodes (DSA) used in electrolysis cells. The DSAs, although electrocatalytically active and stable in long term use, may have limited practical application due to their high material costs. On the other hand, the novel electrocatalysts developed by atomic layer deposition on three-dimensional anodized nanostructures consist of inexpensive metal oxides such as TiO_2 and Al_2O_3 and demonstrate superior wastewater treatment performance compared to the DSAs. They also show high electrocatalytic activities for oxygen evolution reaction, expanding their use for water splitting as well as wastewater treatment. Moreover, I have invented an ultra-portable three-stage ozone-assisted nanofiltration (ULTRON) system, which can be provided to individual or small numbers of homes as decentralized wastewater treatment system. Based on a cost-effective flow-through electrochemical reactor, this system does not depend on biological treatment but only uses an electro-peroxone (E-peroxone) process to effectively remove chemical and biological contaminants from municipal wastewater. The system can reuse treated wastewater to enhance water availability and supply without imposing a detrimental impact on the environment. Reclaimed wastewater can be utilized in a variety of applications, including as makeup water to compensate for water losses in the system and for groundwater discharge.

1.2. Atomic Layer Deposition (ALD)

Recently, the deposition of atomically thin layers (ALD) has emerged as a promising technique for tuning the electronic properties and corresponding activities of semiconductor catalysts. A general ALD process includes sequential alternating pulses of gaseous chemical precursors that react with the functionalized substrate surface.[3] In the first step, a precursor of interest is pulsed into a reactor chamber under vacuum for a specified amount of time to enable the precursor to completely react with the substrate surface, resulting in a saturation layer on the surface (usually less than a monolayer). This step is followed by purging the chamber with an inert carrier gas to clear out any unreacted precursor and/or reaction by-products. Lastly, a counter-reactant precursor is pulsed and then purged in the same fashion, producing up to one layer of the desired material. This process is cycled until the desired film thickness is attained. ALD provides not only conformal coverage over high aspect ratio structures but also thickness control with atomic layer accuracy and precision, and it can be used to control the catalytic activity of a catalyst by tuning its film composition.

However, very little research has been directed at tuning the activity of semiconductor catalysts using ALD. One recent density functional theory (DFT) study has shown the improvement of activity for chlorine evolution reaction (CER) by coating a single atomic layer of TiO_2 on RuO_2 electrodes, indicating that further activity enhancement may be possible with a controlled deposition of TiO_2 (e.g., via ALD).[4] Additional studies have demonstrated that ALD may be used as a tool to tune the surface oxidation state and the catalytic activity of various catalysts for both CER and oxygen evolution reaction (OER), which suggests that ALD may be applied to tune these properties and influence the CER vs. OER selectivity as well.[5]

Herein, black TiO_2 nanotube arrays were deposited with Al_2O_3 via ALD for wastewater treatment and water splitting applications. ALD Al_2O_3 overlayers are known to significantly improve the thermal, mechanical, and chemical stability of TiO_2 nanotube layers.[6] Moreover, one study demonstrates that 30 ALD cycles of Al_2O_3 with a thickness of ~1.5 nm improved the maximum photocurrent density by a factor of 52 and 60% in comparison to pure TiO_2

nanotube arrays and bare quantum dot-sensitized TiO_2 nanotube arrays, respectively.[7] In general, Al_2O_3 ALD incorporates in its process two sequential alternating pulses of H_2O and trimethylaluminum (TMA). The precursors have high reactivity and thermal stability, and only produce methane as a by-product, which does not take part in the deposition process. The following reactions constitute the deposition of Al_2O_3 by ALD:

$$\text{M-OH} + Al(CH_3)_3 \rightarrow \text{M-O-}Al(CH_3)_2 + CH_4,$$
$$\text{M-O-}Al(CH_3)_2 + 2H_2O \rightarrow \text{M-O-Al-}(OH)_2 + 2CH_4,$$

where M represents Ti for initial growth and Al for following cycles.[8] In the first reaction, TMA reacts with the surface hydroxyl group bonded to either Ti or Al and becomes adsorbed onto the surface with one methane molecule as a by-product. In the following reaction, H_2O removes the other two methyl groups from the adsorbed Al-containing species. These two steps continue until the desired thickness of Al_2O_3 is achieved.

This study discussed in Chapter 2 focuses on how the catalytic activity of the CER and the OER can change by tuning black TiO_2 nanotube arrays through Al_2O_3 ALD, and how the observed catalytic tuning effect is correlated with the chemical compositions and electronic properties of the electrocatalysts modified by Al_2O_3 ALD. If successful, highly active electrocatalysts could be used to reduce operation costs for electrochemical wastewater treatment technologies in low- and middle-income countries and to produce hydrogen gas energy-efficiently via water splitting.

1.3. Electro-Peroxone (E-peroxone) Process

Among decentralized wastewater treatment technologies, advanced oxidation processes (AOPs) have attracted increasing interest due to the generation of highly reactive oxidants such as hydroxyl radicals (·OH) that are capable of permanently removing contaminants in wastewater without further treatment for reuse or disposal.[9] Particularly, an electro-peroxone (E-peroxone) process has been considered an attractive AOP option for wastewater treatment, as it demonstrates enhanced ·OH production even in moderate reaction conditions (*e.g.*, circumneutral pH, low ionic strength) in contrast to other AOPs.[10] Therefore, in order to provide an effective yet feasible solution to the water crisis, we have invented an ultra-portable three-stage ozone-assisted nanofiltration (ULTRON) system based on the E-peroxone process.

The ULTRON system can treat domestic wastewater onsite at the point of generation for reuse. Treated wastewater produced from the system is acceptable for non-potable applications such as irrigation and for recycling back into the system to maximize water availability and supply. Based on a cost-effective flow-through electrochemical reactor, the E-peroxone process integrates conventional ozonation with *in situ* hydrogen peroxide (H_2O_2) production. H_2O_2 is electrochemically produced from cathodic oxygen reduction by polytetrafluoroethylene (PTFE)-coated carbon paper electrodes, and subsequently reacts with ozone (O_3) generated from oxygen by an O_3 generator to produce ·OH. To enhance the ·OH production and consequently the treatment efficiency of the system for domestic wastewater, we optimized the mechanical design and process variables by understanding the fundamental reaction mechanisms of the E-peroxone process. Then, we applied the system to treat the following wastewater samples: human urine, synthetic graywater, and primary effluent obtained from a local wastewater treatment plant. For synthetic graywater treatment, we also assessed the recycling capability of the system by reusing treated wastewater instead of fresh electrolyte to produce H_2O_2 for another cycle of treatment.

In the E-peroxone process, cathodic H_2O_2 production usually occurs in the same reaction chamber as ·OH generation. However, the propensity of carbon-based cathodes to degrade in the presence of ·OH poses a challenge for the application of the single-step E-peroxone process. In order to eliminate the potential cathode degradation and provide consistent treatment quality, we modified the design of the system by separating the H_2O_2 production and E-peroxone reacting chamber. In addition to the design modification, we also optimized the operating conditions of the E-peroxone process to improve the treatment performance of the system. We determined the optimal timing and volume of H_2O_2 to be added to the E-peroxone reacting chamber, as excess H_2O_2 in the chamber can experience self-decomposition and even potential oxidation by ·OH.[10] We also determined the optimal flow rate of O_3 into the E-peroxone reacting chamber so that we could have the highest possible O_3 concentration in the solution without significant loss to the chamber headspace. Herein, we report in Chapter 3 that the optimization of the operating conditions enabled the system not only to make the best use of both H_2O_2 and O_3 but also improve the ·OH production for more effective graywater treatment.

CHAPTER 2: Al_2O_3-Coated TiO_2 Nanotube Arrays via Atomic Layer Deposition for Electrochemical Wastewater Treatment and Oxygen Evolution Reaction

2.1. Introduction

Electrochemical oxidation has provided an effective strategy for wastewater treatment, particularly for small-scale decentralized treatment. Unlike large-scale wastewater treatment plants, the treatment systems that rely on electrochemical oxidation as a main source of contaminant degradation and disinfection may not require complex design for interconnected biological, chemical, and physical processes and reactions.[1] Other advantages provided by electrochemical oxidation include high efficiency for chemical oxygen demand (COD) reduction, ease of automated operation, and moderate operating conditions. However, the application of electrochemical oxidation in wastewater treatment can be inhibited by high electrode material/fabrication cost[2] and high energy consumption[3]. Electrodes commonly used for electrochemical oxidation consist of expensive platinum group metals to facilitate the formation of ohmic contact on the base metal substrate.[2] Moreover, the energy consumption of electrochemical oxidation can range from 50 to 1000 kWh per kg of COD removed[4,5], considerably higher than that of aerobic biological treatment (3 kWh/kg COD)[6]. These challenges call for the development of highly active electrocatalysts that are composed of inexpensive earth-abundant metals in order to achieve the cost-effective application of electrochemical wastewater treatment.

Research has been directed at the modification of TiO_2-based substrate to develop an active electrode for energy and environmental applications, replacing the costly electrodes made of IrO_2 and RuO_2 and thereby reducing the electrode material and fabrication costs. TiO_2 has been widely used as a stable and reusable photocatalyst in waster splitting and (waste)water purification owing to its low cost and high photoactivity and stability.[7] However, its large band gap energy (3.2 eV) and high-UV attenuation coefficient in turbid water matrices could pose a major challenge to its effective photocatalytic applications. Some of these unfavorable intrinsic characteristics could be overcome in electrochemical systems where direct photoactivation of TiO_2 is not required. Although TiO_2 has a low electrical conductivity that may hamper its application as an electrocatalyst, surface and interface modification via such techniques as metal/metal oxide doping[8] and coating[9] could be implemented to enhance its electrocatalytic activity by mitigating the Schottky barrier of TiO_2-based substrates.

Self-doping can be used to alter the electronic and catalytic properties of TiO_2. Under a flow of highly active hydrogen species such as H_2 or H_2/Ar at elevated temperatures, TiO_2 nanotube arrays that are fabricated on titanium metal-based surface via anodization become dark black with a smaller band gap.[10] The synthesis of black TiO_2 nanotube arrays concurs with Ti^{3+} and oxygen vacancy formation into TiO_2 lattice.[10] The defects of Ti^{3+} and oxygen vacancies produced through hydrothermal treatment can improve the electrical conductivity of TiO_2[11], therefore leading to its higher electrocatalytic activity for electrochemical oxidation. However, these self-doped TiO_2 nanotube arrays have been observed to deactivate within a few hours of electrocatalysis, resulting from the oxidation of Ti^{3+} centers at high applied anodic potentials and/or poor nanotube structural integrity.[12] Poor electrode stability limits the practical use of TiO_2 nanotube arrays for engineering applications in water splitting and wastewater treatment.

In this study, I have used atomic layer deposition (ALD) to alter the electrochemical properties of black TiO_2 nanotube arrays with varying thickness of Al_2O_3 deposition, and consequently improve their electrocatalytic activity and stability. ALD is a stepwise deposition technique that can achieve uniform and conformal thin films applied with controllable thickness. This technique has been widely used to tune the catalytic and electronic properties of material by depositing thin layers of another material.[9,13,14] Specifically, ALD Al_2O_3 overlayers have been applied for surface recombination passivation, reaction kinetics improvement, and chemical corrosion protection, all of which may synergistically improve their photoelectrochemical performance in visible-light-driven applications.[15–17] Moreover, it has been demonstrated that thin ALD Al_2O_3 coatings significantly enhance the thermal, chemical, and mechanical stability of TiO_2 nanotube layers.[18] Despite active research conducted on ALD surface treatment, an electrochemical performance using a conformal Al_2O_3 overlayer on black TiO_2 nanotube arrays has been less explored.

Herein, the electrochemical oxidation activities of black TiO_2 nanotube arrays with different thickness of Al_2O_3 overlayers were evaluated for the chlorine evolution reaction (CER; a key reaction in wastewater treatment) and the oxygen evolution reaction (OER; a limiting half-reaction of water splitting). Black TiO_2 nanotube arrays with 8 ALD cycles of Al_2O_3 demonstrated 3-fold enhancements of electrochemical active surface area (ECSA) for the CER and the OER compared to bare substrates without Al_2O_3 deposition. Furthermore, they showed superior performance of electrochemical oxidation for wastewater treatment than an IrO_2-based dimensionally stable anode.

2.2. Experimental Section

2.2.1. Electrode Preparation

A 2 cm x 1.5 cm Ti plate with thickness of 0.5 mm was used as a base substrate. To start with TiO_2 nanotube array electrode fabrication, the plate was surface cleaned with HF/HNO_3 mixture and anodized in ethylene glycol electrolyte with 2 wt % H_2O and 0.25 wt % NH_4F for 6 hours at an applied voltage of 42 V. The resulting amorphous TiO_2 nanotube arrays were subsequently deposited with varying ALD cycles of Al_2O_3, followed by hydrothermal treatment.

Al_2O_3 films were deposited on amorphous TiO_2 nanotube arrays using an Ultratech Fiji 200 Plasma ALD machine. The ALD process was run at 150 ^{o}C in exposure mode. In this mode, the stop valve was closed before ALD precursor introduction so that the pulsed precursors could stay longer reacting with the amorphous TiO_2 nanotube array substrate in the reaction chamber. First, one 0.030 sec pulse of H_2O was introduced and stayed in the chamber for 15 sec, followed by a 15 sec purge of N_2 gas at a constant flow rate of 0.13 L/min with the stop valve open to clear out any unreacted precursor and byproducts. Subsequently, one 0.015 sec pulse of trimethylaluminum (TMA) was applied to the substrate and remained in the chamber for 15 sec, followed by the same N_2 purge step. This two-reaction cycle of ALD was repeated until the desired thickness of Al_2O_3 deposition was achieved. In this study, the following ALD cycles of Al_2O_3 were prepared: 0 (without any Al_2O_3 deposition), 3, 5, 8, 15, 20, 30, and 40 cycles.

Lastly, the TiO_2 nanotube arrays with and without Al_2O_3 deposition went through hydrothermal treatment in a tube furnace to obtain black TiO_2 nanotube arrays. They were annealed at 450 ^{o}C under a constant 5% H_2/Ar flow at 0.3 L/min for 30 min and then naturally cooled down to room temperature. **Figure 1** shows how the TiO_2 nanotube array electrode changes visually after each synthesis step.

2.2.2. Electrode Characterization

The electrochemical properties of black TiO_2 nanotube arrays with varying ALD cycles of Al_2O_3 were characterized using a Biologic VSP-300 potentiostat. All the electrochemical tests were conducted in a three-electrode configuration with stainless steel as a counter electrode and saturated Ag/AgCl as a reference electrode under continuous stirring. Prior to data collection for CER and OER activity measurements, nitrogen gas or oxygen gas was bubbled through the CER or OER electrolyte, respectively, for at least 5 min.

Cyclic voltammetry (CV) was measured with a scan rate of 10 mV/s for the CER in 5 M NaCl adjusted to pH 2 with HCl and the OER in 1 M H_2SO_4 and 100 mM potassium phosphate buffer solution (KPi) at pH 7.2. Based on the CV measurements, overpotentials were determined at current densities of 1 mA/cm^2 and 10 mA/cm^2 for black TiO_2 nanotube arrays as a function of the number of Al_2O_3 ALD cycles (Some substrates with thicker Al_2O_3 overlayers were not able to achieve the current density of 10 mA/cm^2 within a given range of applied voltage in CVs). All the anodic potentials measured in this study were corrected for the IR drop by measuring the solution resistance (R_u) of each electrolyte using electrochemical impedance spectroscopy ($R_u = 3.8 \pm 0.1\ \Omega$ in 5 M NaCl at pH 2, $1.9 \pm 0.3\ \Omega$ in 1 M H_2SO_4, and $2.9 \pm 0.6\ \Omega$ in 100 mM KPi at pH 7.2).

In addition to overpotential measurements, electrochemically active surface area (ECSA) was determined for the CER and the OER as a function of the number of Al_2O_3 ALD cycles on black TiO_2 nanotube arrays. ECSA can be calculated by dividing the double layer capacitance (C_{dl}) by the specific capacitance (C_s).[19] For the CER, C_{dl} was measured in 5 M NaCl at pH 2 via electrochemical impedance spectroscopy (EIS) at the open-circuit potential (E_{oc}). The EIS equivalent circuit model for black TiO_2 nanotube arrays with Al_2O_3 deposition was characterized by a Randles circuit where a resistor is in series with a parallel combination of a capacitor and a shunt resistor (described in the following equation: $R_u + C_{dl}/R_{ct}$ where R_u is the solution resistance and R_{ct} is the charge transfer resistance). C_{dl} was measured based on the fitting of EIS data by the Randles circuit. On the other hand, for the OER, C_{dl} was determined in 1 M H_2SO_4 by plotting the measured capacitive currents as a function of CV scan rate, and the slope of the linear best-fit line from the plot was taken as C_{dl}. The acidic electrolytes used for the CER and the OER were reported to have the C_s of 0.035 mF/cm^2.[19]

Black TiO_2 nanotube arrays with 0, 8, and 30 ALD cycles of Al_2O_3 were chosen based on the overpotential and ECSA measurements, and further examined to characterize their electrical properties and morphologies for comparison. Nyquist and Mott-Schottky plots were determined via EIS in 0.1 M $NaClO_4$. Nyquist plots were fit to the Randles circuit to measure the charge transfer resistance. Moreover, ZEISS 1550VP field emission scanning electron microscopy (SEM) was used to characterize the nanotube surface features and evaluate the morphological changes such as the nanotube diameter resulted from the deposition of Al_2O_3. Prior to SEM imaging, 7 nm of Au was deposited onto the substrates via a spin coater to prevent charge-up effects. The nanotube diameter of each substrate was estimated using ImageJ software.

2.2.3. X-ray Photoelectron and Absorption Spectroscopy

Laboratory-based X-ray photoelectron spectroscopy (XPS) was conducted using non-monochromatized Mg K_α (1253.56 eV) excitation and a ScientaOmicron Argus CU electron analyzer with a pass energy of 20 eV and total energy resolution of 0.9 eV. The base pressure was at 3 x 10^{-9} mbar in the XPS analysis chamber. Moreover, synchrotron-based hard X-ray photoelectron spectroscopy (HAXPES) was performed at the High Kinetic Energy Photoelectron Spectrometer (HiKE) end-station at the BESSY II KMC-1 beamline at Helmholtz-Zentrum Berlin using a VG Scienta R4000 hemispherical electron energy analyzer. HAXPES spectra were recorded with different excitation energies depending on the element of interest. For surface sensitive measurements, 530 eV, 600 eV, and 145 eV were used for Ti 2p, O 1s, and Al 2p core levels, respectively, whereas 1250 eV, 1330 eV, and 874 eV used for bulk sensitive measurements. The base pressure was less than 10^{-8} mbar in the analysis chamber. For all the HAXPES measurements, the total energy resolution was maintained approximately at 0.25 eV with a pass energy of 100 eV. The binding energy scale for both the lab-based XPS and synchrotron-based HAXPES measurements was calibrated by measuring the Au $4f_{7/2}$ peak of a grounded clean Au foil and adjusting the binding energy of Au $4f_{7/2}$ to 84.00 eV. All the measured XPS spectra were analyzed using the WinSpec program with a Shirley background and mixed singlet signal.

X-ray absorption spectroscopy (XAS) was conducted at the same HiKE end-station in total electron yield (TEY) mode. The photon energy was scanned from 455 to 475 eV to measure the Ti L-edge XAS spectra of black TiO_2 nanotube arrays with varying deposition thickness of Al_2O_3.

2.2.4. Wastewater Treatment

Toilet wastewater obtained from the pilot scale toilet system installed at the California Institute of Technology (Caltech) was used to evaluate the wastewater treatment performance of black TiO_2 nanotube arrays with 8 ALD cycles of Al_2O_3. The pH of the wastewater was around 8.0, and the conductivity ranged from 3.2 to 3.4 mS/cm. The initial concentrations of chemical oxygen demand (COD) and ammonium (NH_4^+) in the wastewater were 275 mg/L and 83 mM, respectively. The treatment performance was assessed in terms of COD and NH_4^+ reductions over 5-hour electrolysis. COD was measured via colorimetry following Hach Method 8000, whereas NH_4^+ measured via ion chromatography. Electrolysis was conducted at the current density of 10 mA/cm^2 with the ratio of electrode area to wastewater volume of 60 m^{-1}. A commercial IrO_2 dimensionally stable anode (DSA) (Nanopac, South Korea) was tested in the same operating conditions for comparison.

Furthermore, free chlorine and hydroxyl radical productions were measured via HPLC (Agilent) equipped with a Zorbax XBD column and Hach method 10102 with a DPD (*N*,*N*-diethyl-*p*-phenylenediamine) reagent. Free chlorine production was performed in 50 mM NaCl at the current density of 10 mA/cm^2 for 10 min. The current efficiency of CER was also determined based on the produced free chlorine concentration. On the other hand, benzoic acid (BA) was used as a probe molecule for hydroxyl radical production. The initial concentration of BA was 5 mM in 30 mM $NaClO_4$ electrolyte, and its concentration was measured every 30 min during 2-hour electrolysis at the applied current density of 10 mA/cm^2.

2.3. Results and Discussion

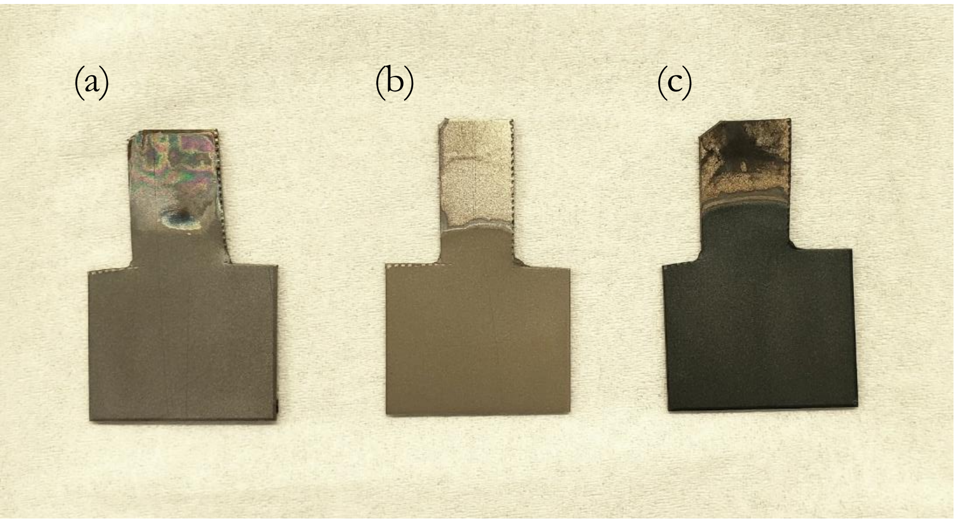

Figure 1. TiO_2 nanotube arrays on a Ti metal plate after each synthesis step. (a) Amorphous TiO_2 nanotube arrays after anodization. (b) Amorphous TiO_2 nanotube arrays with Al_2O_3 overlayer after ALD. (c) Black TiO_2 nanotube arrays with Al_2O_3 ALD after hydrothermal treatment. *Note: Regardless of Al_2O_3 ALD, the black TiO_2 nanotube array substrate remained black after annealing under 5% H_2/Ar atmosphere.

After TiO_2 nanotube array fabrication and ALD, SEM was used to characterize the nanotube surface features and evaluate the morphological changes such as the nanotube diameter resulted from the deposition of Al_2O_3. **Figure 2 (a) and (b)** show the structures of amorphous TiO_2 nanotube arrays that have not yet gone through hydrothermal treatment and ALD. The nanotube pores are readily observed from top view, whereas the cylindrical characteristics of nanotubes from side view. The inner diameter of amorphous TiO_2 nanotube arrays was estimated to be 73.8 ± 5.7 nm (7 nm of Au deposited before SEM to prevent charge-up effects was subtracted). Black TiO_2 nanotube arrays share the same nanotube surface features in the top and side views with an estimated pore diameter of 73.4 ± 4.1 nm, which indicates that hydrothermal treatment does not change the nanotube pore diameter. On the other hand, the deposition of Al_2O_3 onto TiO_2 nanotube arrays led to decreasing pore size, as shown in **Figure 2 (c), (d), and (e)**. 8 ALD cycles of Al_2O_3 reduced the pore diameter to 71.0 ± 6.3

nm, while the diameter shrunk to 61.1 ± 5.9 nm with 30 ALD cycles and to 36.4 ± 4.9 nm with 100 ALD cycles.

It was observed that the nanotube pore size decreased with increasing ALD cycle. **Figure 3** shows the linear relationship between the pore size and the number of ALD cycle. Based on this linear trend, the deposition rate of Al_2O_3 onto TiO_2 nanotube arrays was estimated to be 0.35 nm/cycle. For this study, I tried to characterize the cross sections of TiO_2 nanotubes, particularly to verify the uniform, conformal deposition of Al_2O_3 on the inner nanotube walls. However, Ti plates onto which TiO_2 nanotube arrays were developed were too malleable to be cleaved into clean pieces without distorting the nanotube structures. In future studies, more advanced metal cutting techniques such as plasma and waterjet can be applied to ensure a clean cut of Ti plate while maintaining the nanotube structures. By doing so, we can examine the interior surfaces of TiO_2 nanotubes and make sure the uniform, conformal coverage of Al_2O_3 ALD on the nanotube inner walls via SEM and energy-dispersive X-ray spectroscopy (EDS).

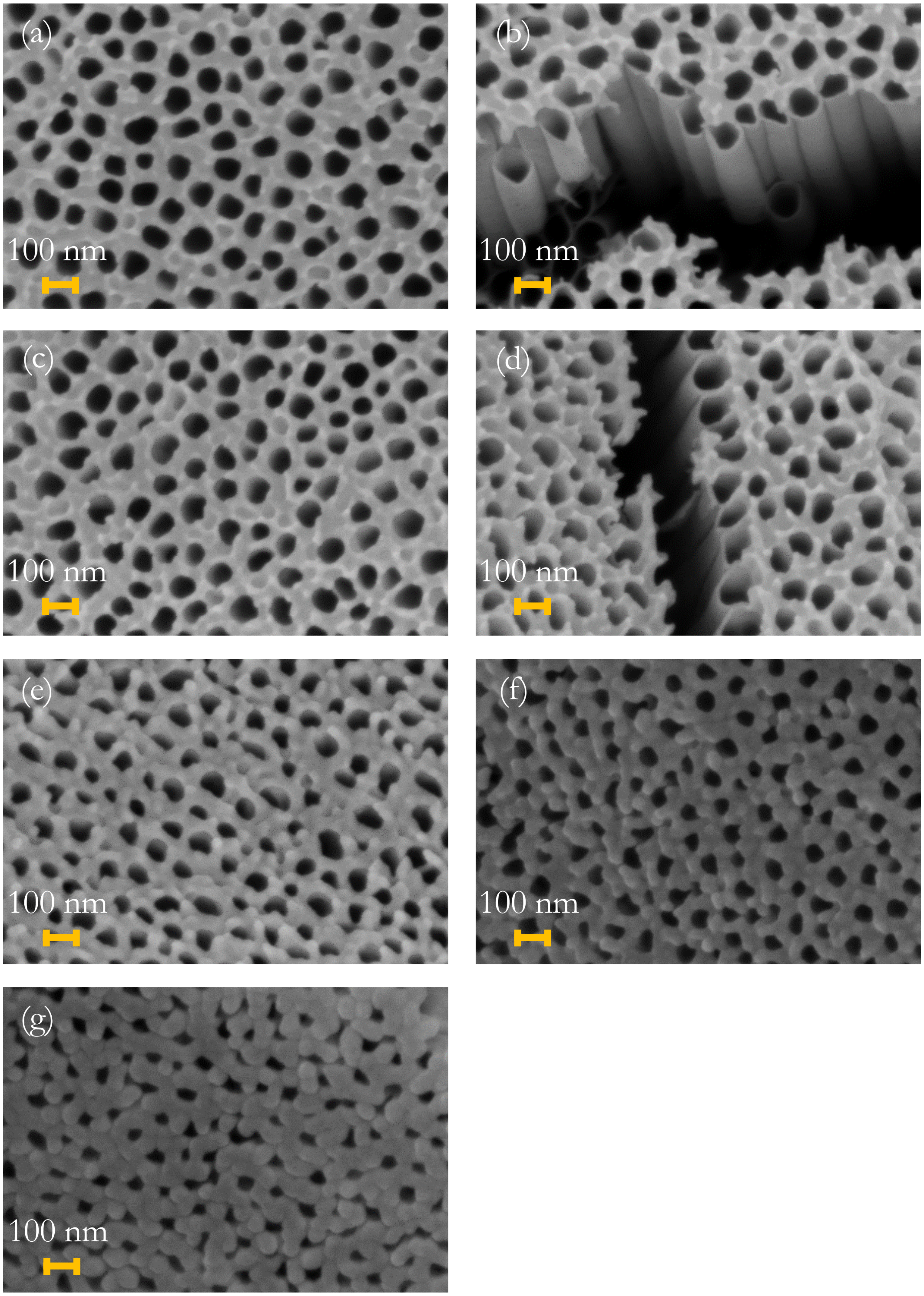

Figure 2. SEM images of amorphous and black TiO_2 nanotube arrays with Al_2O_3 ALD. (a) Top and (b) side view of amorphous TiO_2 nanotube arrays. (c) Top and (d) side view of black TiO_2 nanotube arrays without Al_2O_3 ALD. Top views of black TiO_2 nanotube arrays with (e) 8 cycles, (f) 30 cycles, and (g) 100 cycles of Al_2O_3 ALD.

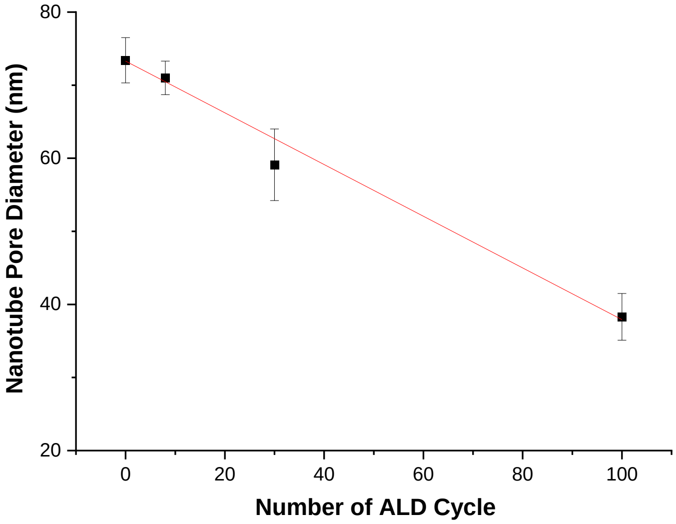

Figure 3. Black TiO_2 nanotube pore diameter (nm) as a function of Al_2O_3 ALD cycle. The slope of the linear best-fit line is -0.35 nm/cycle (linear growth rate = 0.35 nm/cycle) with $r^2 = 0.99$.

CV was used to measure the electrochemical activity of black TiO_2 nanotube arrays with varying ALD cycles of Al_2O_3 in 5 M NaCl at pH 2 for the CER and in 1 M H_2SO_4 and 100 mM KPi at pH 7.2 for the OER. The test electrode potential was increased in the anodic direction to determine the anodic branch current responses for the CER and the OER. The strongest current responses were observed with 8 ALD cycles of Al_2O_3 for both reactions. In order to investigate the effect of Al_2O_3 ALD on the electrochemical activity, CVs of 8 ALD cycles were compared to those of 0 ALD cycle (bare black TiO_2 nanotube arrays) in **Figure 4**. The measured current densities were normalized to the geometric surface area of electrode (6 cm^2). The substrate with 8 ALD cycles shows lower onset potentials and higher current densities for both the CER and OER than bare black TiO_2 nanotube arrays. This catalytic enhancement confirms the favorable effect of Al_2O_3 ALD on the CER and OER activities of black TiO_2 nanotube arrays. For example, 8 ALD cycles resulted in approximately 5 times higher current density at 3.1 V_{RHE} for the CER than 0 cycle ALD. Applying ALD to overcoat black TiO_2 nanotube arrays with Al_2O_3 is expected to alter their electrical properties (e.g., conductivity) and therefore enhance their CER and OER electrochemical activities.

(a) CER in 5 M NaCl at pH 2

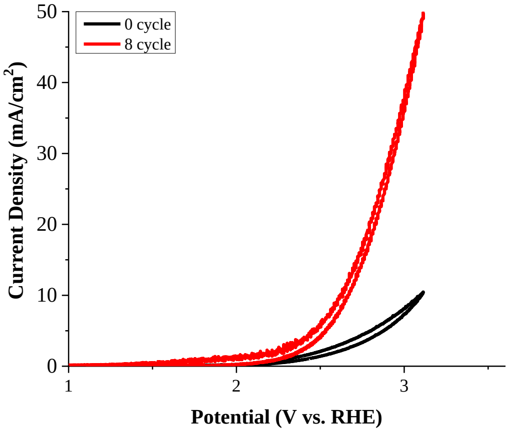

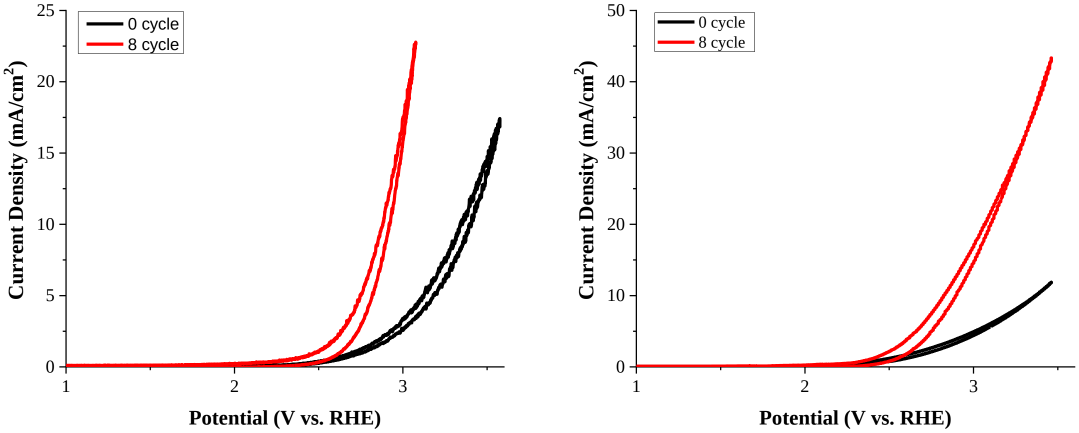
(b) OER in 1 M H_2SO_4

(c) OER in 100 mM KPi at pH 7.2

Figure 4. CVs of black TiO_2 nanotube arrays with 0 and 8 ALD cycles of Al_2O_3 in (a) 5 M NaCl at pH 2 for the CER and in (b) 1 M H_2SO_4 and (c) 100 mM KPi at pH 7.2 for the OER. The current density was normalized to the geometric surface area of electrode (6 cm^2).

Overpotentials were also measured at current densities of 1 mA/cm^2 and 10 mA/cm^2 to determine the electrochemical activity of black TiO_2 nanotube arrays as a function of Al_2O_3 ALD cycles for the CER and OER. Some substrates with higher ALD cycles showed anodic branch current responses too weak to achieve the current density of 10 mA/cm^2. At the current densities, the overpotential initially decreased for both the CER and the OER as the number of ALD cycle increased, reaching the lowest at 8 ALD cycle. However, higher ALD cycles resulted in greater CER and OER overpotentials, overall exhibiting a volcano plot between the overpotential and the number of Al_2O_3 ALD cycle that illustrates the Sabatier principle.[20] For the CER, the overpotential reductions between 8 cycles and bare black TiO_2 nanotube arrays (0 cycle) were 360 mV at 1 mA/cm^2 and 465 mV at 10 mV/cm^2. For the OER in 1 M H_2SO_4 and 100 mM KPi at pH 7.2, the overpotentials decreased by 465 mV and 121 mV at 1 mA/cm^2 and 480 mV and 570 mV at 10 mA/cm_2, respectively, with 8 ALD cycles of Al_2O_3. When the deposition thickness of Al_2O_3 was equal to or greater than 20 cycles, the overpotential significantly increased compared to bare black TiO_2 nanotube arrays for both the CER and OER. This electrochemical activity loss indicates that Al_2O_3 coatings serve as passivation layers when they reach certain thickness.

This volcano-shaped trend of electrochemical activity as a function of the number of ALD cycle was observed for ECSA measurements as well. In general, ECSA is considered an estimation of electrochemically active sites, and is proportional to the C_{dl}.[21,22] For the CER, C_{dl} was derived from Nyquist plots with the Randles circuit as an equivalent circuit model, whereas C_{dl} for the OER was measured by plotting the capacitive currents as a function of scan rate and extracting the slopes of linear best-fit lines (**Figure 6**). ECSA for the CER and the OER increased at first with the higher number of ALD cycles and decreased drastically after reaching its maximum at 8 cycles (**Figure 7**). The same volcano-shaped trends of overpotential and ECSA measurements indicate that higher electrochemical activities of black TiO_2 nanotube arrays with Al_2O_3 ALD could be ascribed to the generation of more CER and OER active sites. 8 ALD cycles of Al_2O_3 enlarged the ECSA 3-fold for the CER and the OER compared to bare TiO_2 nanotube arrays. In other words, the total number of electrochemical active sites was the highest with 8 ALD cycles, which corroborates the lowest CER and OER overpotentials observed in **Figure 5**. The concentrations of active sites may not be as high with lower ALD cycles as they may not be able to produce uniform, conformal overlayers of Al_2O_3 on black TiO_2 nanotube arrays. Higher ALD cycles, on the contrary, yield much thicker deposition of Al_2O_3 that may function as surface passivation and impede the production of electrochemical active sites.

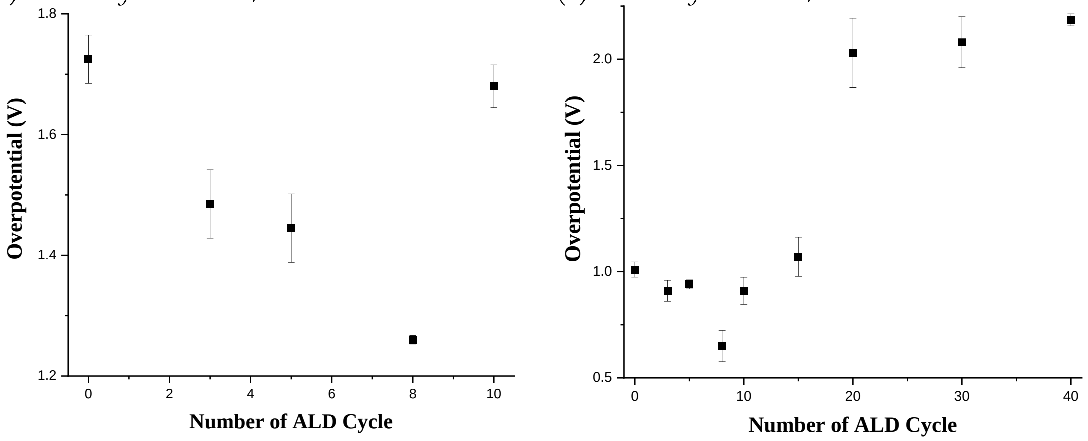
(a) CER at $j = 10$ mA/cm^2 in 5 M NaCl

(b) CER at $j = 1$ mA/cm^2 in 5 M NaCl

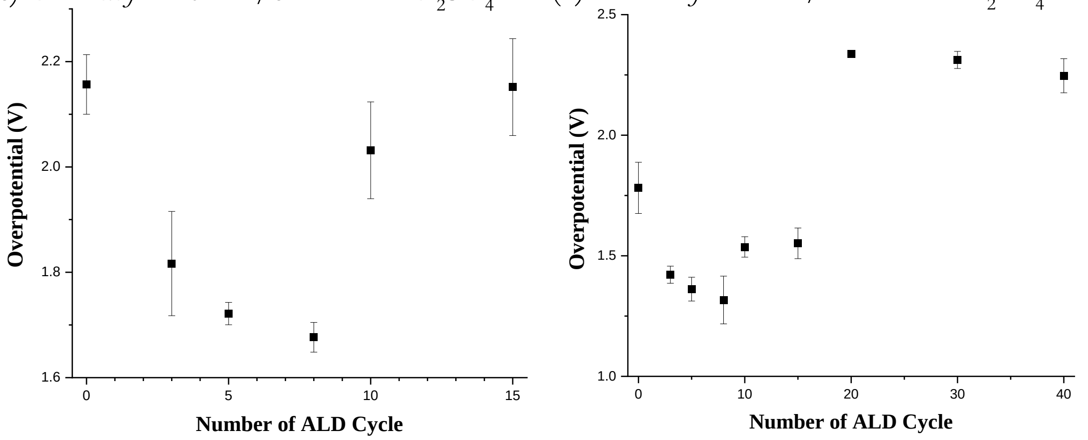
(c) OER at $j = 10$ mA/cm^2 in 1 M H_2SO_4

(d) OER at $j = 1$ mA/cm^2 in 1 M H_2SO_4

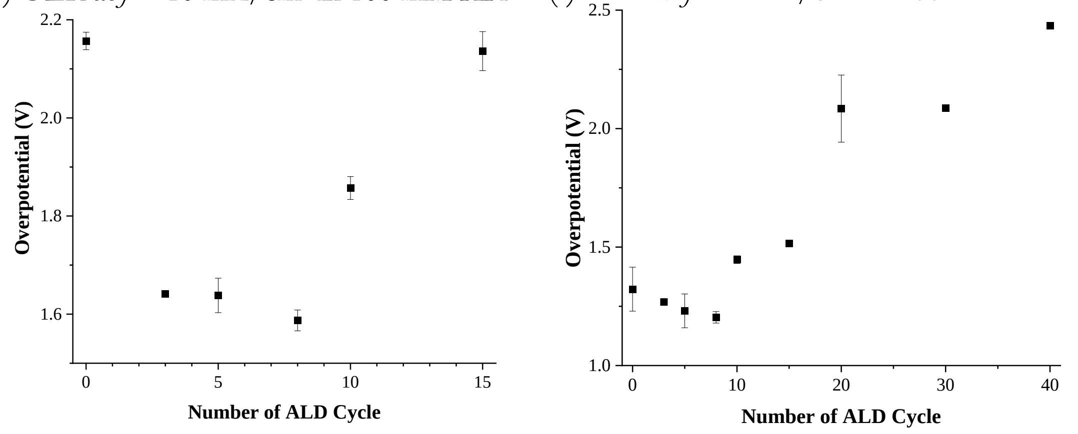
(e) OER at $j = 10$ mA/cm^2 in 100 mM KPi

(f) OER at $j = 1$ mA/cm^2 in 100 mM KPi

Figure 5. Overpotential measurements at current densities (j) of 1 mA/cm^2 and 10 mA/cm^2 for the CER in 5 M NaCl and for the OER in 1 M H_2SO_4 and 100 mM KPi at pH 7.2.

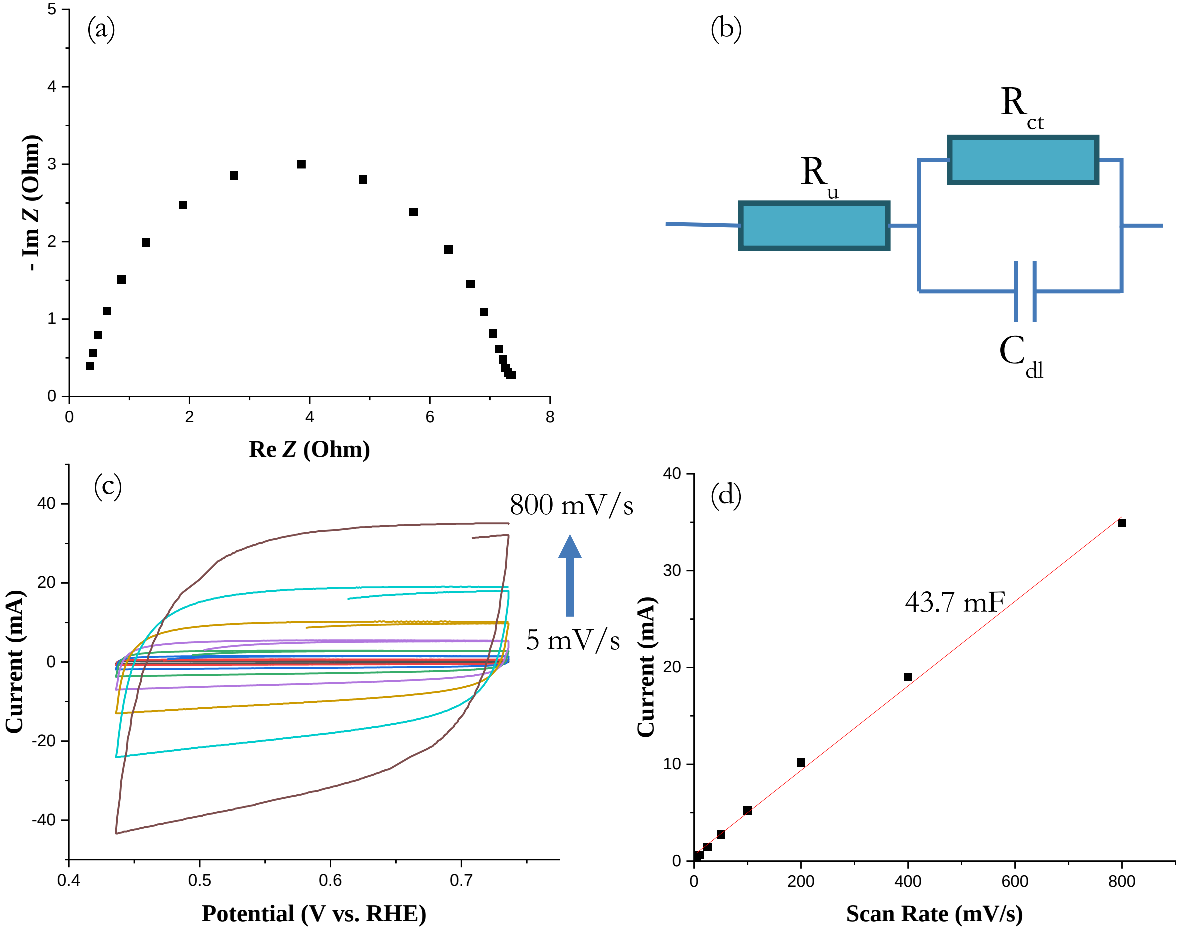

Figure 6. (a) Example Nyquist plot of black TiO_2 nanotube arrays with 8 ALD cycles in 5 M NaCl at pH 2. The C_{dl} for the CER was determined by using (b) Randles equivalent circuit to fit the EIS spectrum. (c) Example linear sweep voltammograms of 8 ALD cycles in 1 M H_2SO_4 at 8 different scan rates: 5, 10, 25, 50, 100, 200, 400, and 800 mV/s. The C_{dl} for the OER was determined by extracting the slope of the linear fit from (d) the plot of capacitive currents measured from the linear sweep voltammograms as a function of scan rate.

The observed enhancement in electrochemical performance (**Figures 4 and 5**) could be attributed not only to the increase in ECSA but also to the improvement in intrinsic electrocatalytic activity. In order to separate the two effects and assess the influence of Al_2O_3 ALD on the intrinsic activity of black TiO_2 nanotube arrays, the measured current densities were normalized by ECSA (**Figure 8**). Although the extent of enhancement in ECSA-normalized current density was less considerable compared to **Figure 4**, black TiO_2 nanotube arrays with 8 cycles still exhibited lower onset potentials and higher current densities than 0 cycle, thereby demonstrating higher intrinsic activities in CER and OER. Therefore, 8 ALD cycles of Al_2O_3 resulted in enlarged electroactive surface area and enhanced intrinsic electrocatalytic activity, both contributing to the improvement in electrochemical performance for the CER and the OER. According to XPS data (shown later), the deposition of Al_2O_3 facilitated the generation of oxygen vacancies, which led to enlarged ECSA. However, further research is needed to provide the evidence of intrinsic activity enhancement by examining the electronic properties (e.g., surface charge density[9]) of black TiO_2 nanotube arrays with Al_2O_3 ALD.

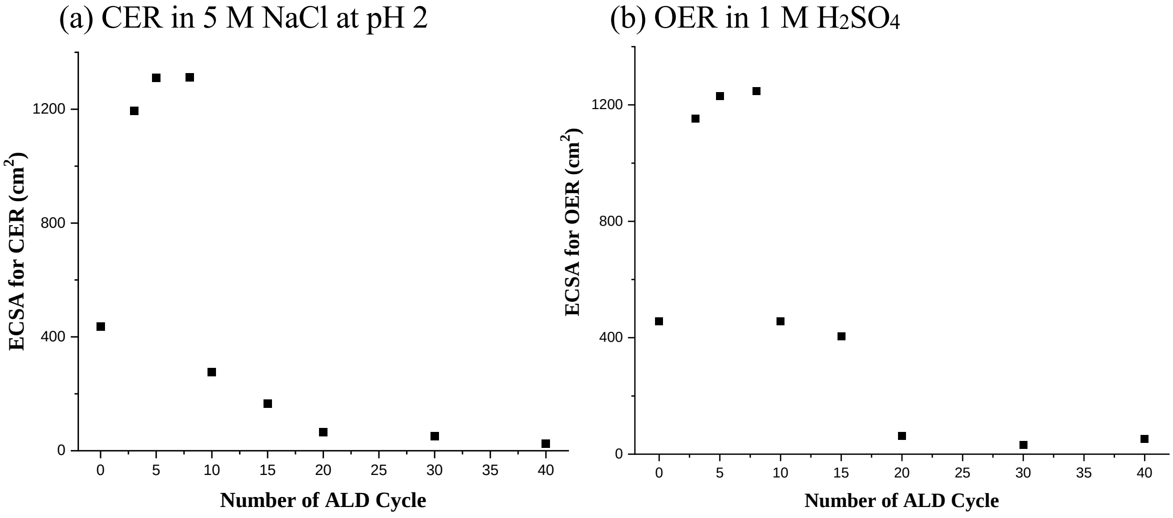

Figure 7. ECSA measurements for (a) the CER and (b) the OER as a function of the number of ALD cycle.

Furthermore, the deposition of Al_2O_3 improved the electrical conductivity of black TiO_2 nanotube arrays. EIS was used to analyze the charge transfer characteristics with and without Al_2O_3 ALD. In the Nyquist plots (**Figure 9 (a)**), black TiO_2 nanotube arrays with 0 cycle, 8 cycles, and 30 cycles displayed distinct semi or quarter circular arcs. The arc size in the Nyquist plot fit by a Randle circuit is proportional to the charge transfer resistance of electrode. The substrate with 8 cycles exhibited the smallest arc size, followed by 0 cycle and 30 cycles, owing to the enhanced interfacial charge transfer. This result suggests that 8 ALD cycles of Al_2O_3 enabled more efficient electron transport through TiO_2 nanotube networks. Mott-Schottky plots also validated the principal role of Al_2O_3 ALD in the improved electrical conductivity of black TiO_2 nanotube arrays. As shown in **Figure 8 (b)**, the substrate with 8 cycles showed the most flat slope of Mott-Schottky plot, indicating an enhancement in electrical conductivity.[23] 8 ALD cycles of Al_2O_3 could promote the formation of Ti^{3+} sites and oxygen vacancies on TiO_2, redistributing excess electrons for charge balance between the oxygen vacancies and neighboring Ti atoms and consequently enhancing the charge carrier density.[24] Although Al_2O_3 overlayers may function as electrical insulation, the thickness of 8 ALD cycles (~2 nm) would be thin enough for electrons to tunnel to TiO_2 via Al_2O_3 coatings and thick enough to prevent oxygen from re-oxidizing Ti^{3+} or reacting with oxygen vacancies when exposed to air.[25,26] In contrast, 30 ALD cycles could produce Al_2O_3 insulating layers that would impede the effective charge transport and therefore reduce the electrical conductivity.

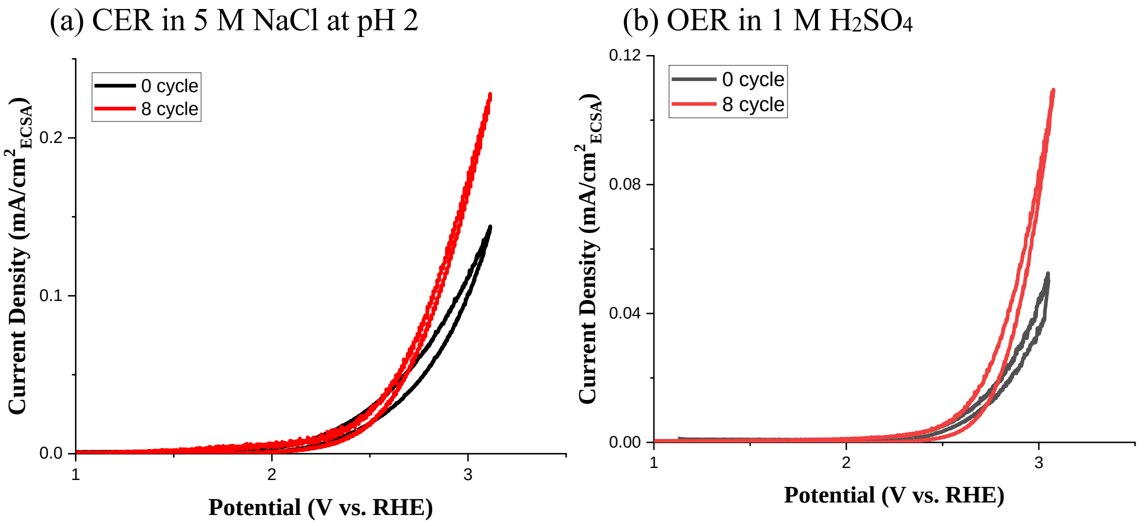
(a) CER in 5 M NaCl at pH 2

(b) OER in 1 M H_2SO_4

Figure 8. Current densities normalized to ECSA for the CER and the OER. The ECSA-normalized current densities were compared between 0 cycle and 8 cycles.

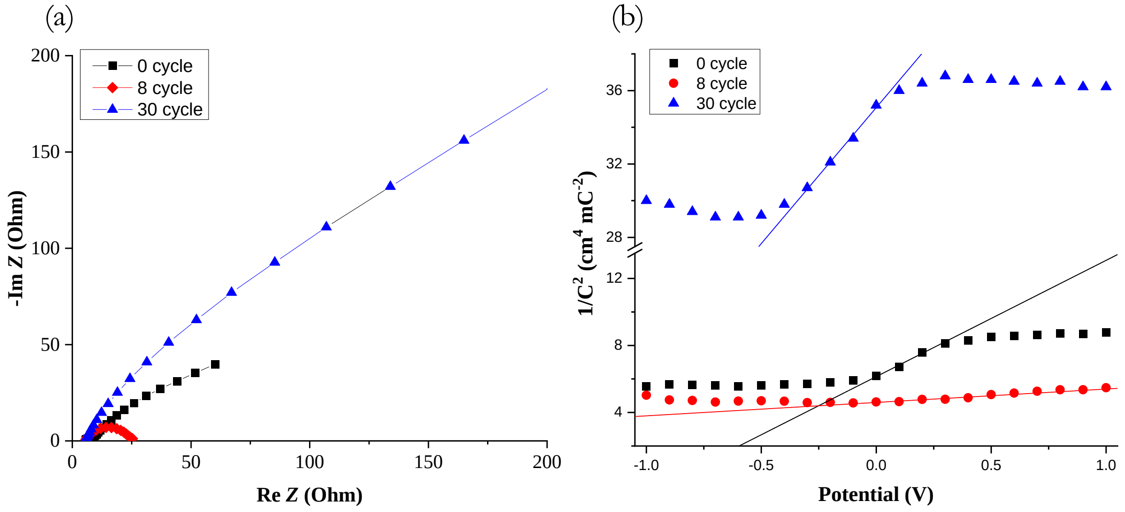

Figure 9. (a) Nyquist and (b) Mott-Schottky plots of 0 cycle, 8 cycles, and 30 cycles in 0.1 M $NaClO_4$.

Electrochemical and thermal reduction is regarded as a facile and effective method to induce the self-doping of Ti^{3+} and the introduction of oxygen vacancies into TiO_2.[8,27] The induced Ti^{3+} and oxygen vacancies could improve the electrochemical performance of TiO_2-based electrode by facilitating bulk conductivity and increasing the number of electrochemical active sites.[8,27] XPS measurements of the Ti 2p and O 1s core levels confirmed the presence of Ti^{3+} and oxygen vacancies on black TiO_2 nanotube arrays with 0 cycle, 8 cycles, and 30 cycles of Al_2O_3 ALD. Particularly, the surface sensitive Ti 2p XPS spectrum of 8 cycles (**Figure 10 (a)**) displays a shoulder peak at around 458 eV, which corresponds to the existence of Ti^{3+}, although this peak is almost unnoticeable in the bulk sensitive spectrum of 8 cycles (**Figure 10 (d)**). Compared to 0 cycle, both the O 1s and Al 2p peaks in the surface sensitive XPS measurements are shifted to lower binding energies possibly due to the deposition of Al_2O_3. In fact, the shift is more considerable for 30 cycles. This pattern is observed for the bulk sensitive measurements as well.

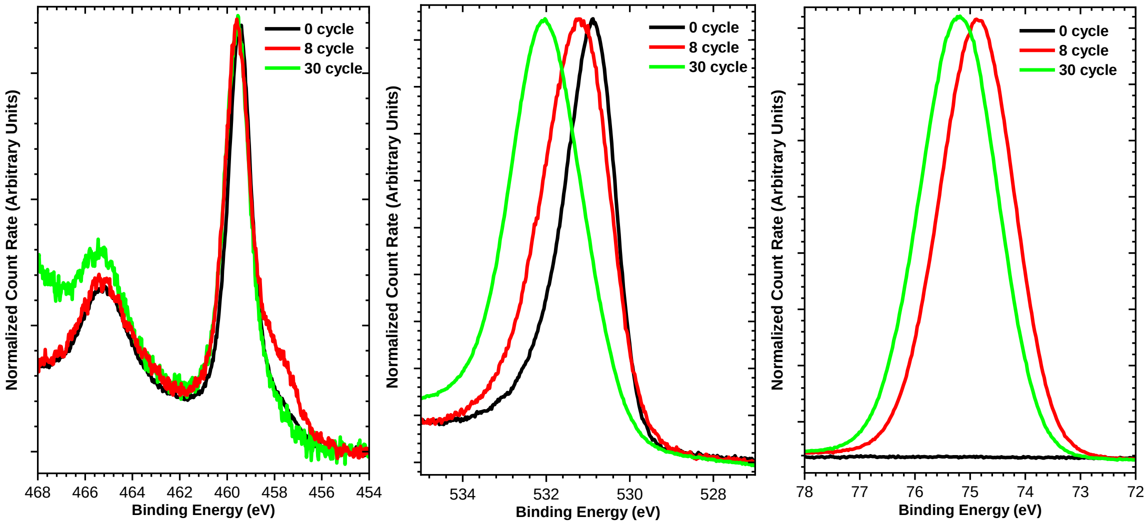

(a) Ti 2p surface (b) O 1s surface (c) Al 2p surface

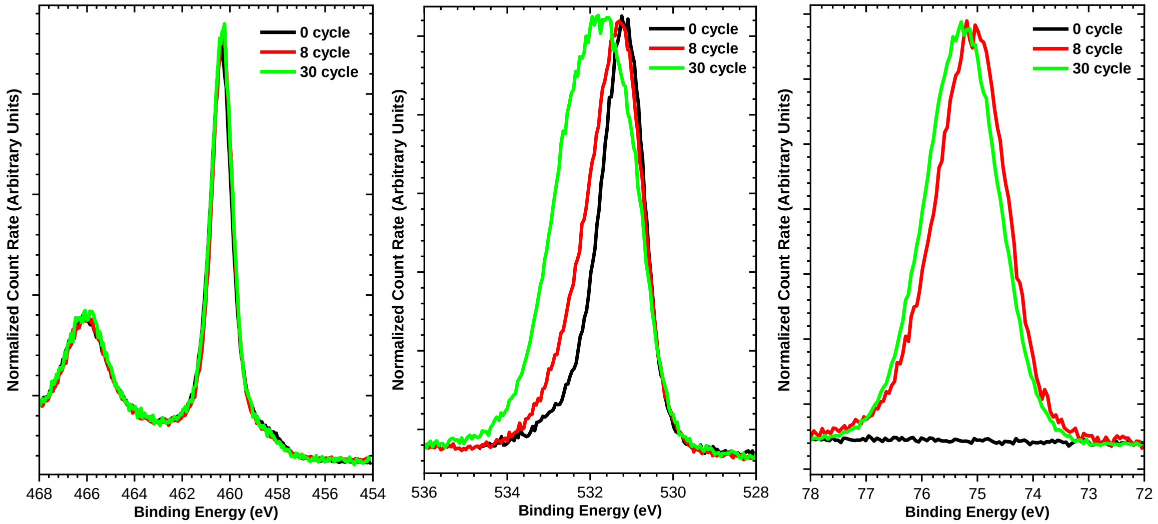

(d) Ti 2p bulk (e) O 1s bulk (f) Al 2p bulk

Figure 10. Surface (top) and bulk (bottom) sensitive XPS measurements for (a,d) Ti 2p, (b,e) O 1s, and (c,f) Al 2p core levels of black TiO_2 nanotube arrays with 0 cycle, 8 cycles, and 30 cycles.

The standard binding energy of Ti^{4+} in the Ti $2p_{3/2}$ peak of TiO_2 is recorded at 459.5 eV.[28,29] However, if TiO_2 contains some amount of Ti^{3+} in the surface or bulk, its Ti $2p_{3/2}$ peak turns into much broader potentially with a shoulder peak as shown in **Figure 10 (a)**. The observed shoulder peak at a lower binding energy of 458.1 eV is related to a more reduced Ti state, namely Ti^{3+}. The Ti 2p core level XPS measurements (**Figure 11**) were analyzed with peak fitting to determine the relative contents of Ti^{3+} in the surface and bulk of reduced TiO_2. Black TiO_2 nanotube arrays with 8 cycles comprised the most amount of Ti^{3+} in the surface (38%), followed by 0 cycle (20%) and 30 cycles (15%). On the other hand, the presence of Ti^{3+} was negligible in the bulk regardless of Al_2O_3 ALD thickness, indicating that the reduction of Ti^{4+} would occur mostly in the surface or sub-surface. It was reported that hydrothermal treatment could introduce surface disorders and consequently Ti^{3+} defects in TiO_2.[30] Moreover, Al_2O_3 ALD could promote the reduction of Ti^{4+} to Ti^{3+} in the sub-surface as the TMA precursor creates (O-Al) bonds with oxygen atoms on the surface by breaking their bonds with the Ti.[31] In general, the generation of Ti^{3+} defects concurs with the introduction of oxygen vacancies into the TiO_2 lattice as observed in the O 1s core level XPS measurements.

The XPS spectra of O 1s core level were deconvoluted into three characteristic peaks of lattice oxygen (O^{2-}) at 530-531 eV, adsorbed oxygen (O_{ads}) at 531.1-531.6 eV, and hydroxyl groups (OH) at 532-533 eV.[8,32] The peak ascribed to the adsorbed molecular water was neglected here as all the samples were annealed in vacuum at 400 ^{o}C for 30 min before XPS measurements. Resulted from the dissociative adsorption of molecular oxygen onto oxygen vacancies, the O_{ads} could be measured to indirectly determine the amount of oxygen vacancies. Based on this correlation, black TiO_2 nanotube arrays with 8 cycles contained the highest concentration of oxygen vacancies (41%) in the surface, followed by 0 cycle (31%) and 30 cycles (25%) (**Figure 12**). The same trend was seen for the bulk measurements. Moreover, it was observed that the concentration of hydroxyl groups in the surface increased with the number of ALD cycles: 0 cycle (9%) < 8 cycles (15%) < 30 cycles (57%). Considering the water molecules were removed during annealing, the hydroxyl groups were mostly originated from Al-OH bonds formed during the Al_2O_3 ALD process. The process utilized cycles of alternating precursors (i.e., TMA and H_2O). Not only did 30 cycles exhibit the thickest Al_2O_3 overlayer, but they could also have most conformal coverage on TiO_2 nanotube networks, accounting for their highest hydroxyl group concentration.

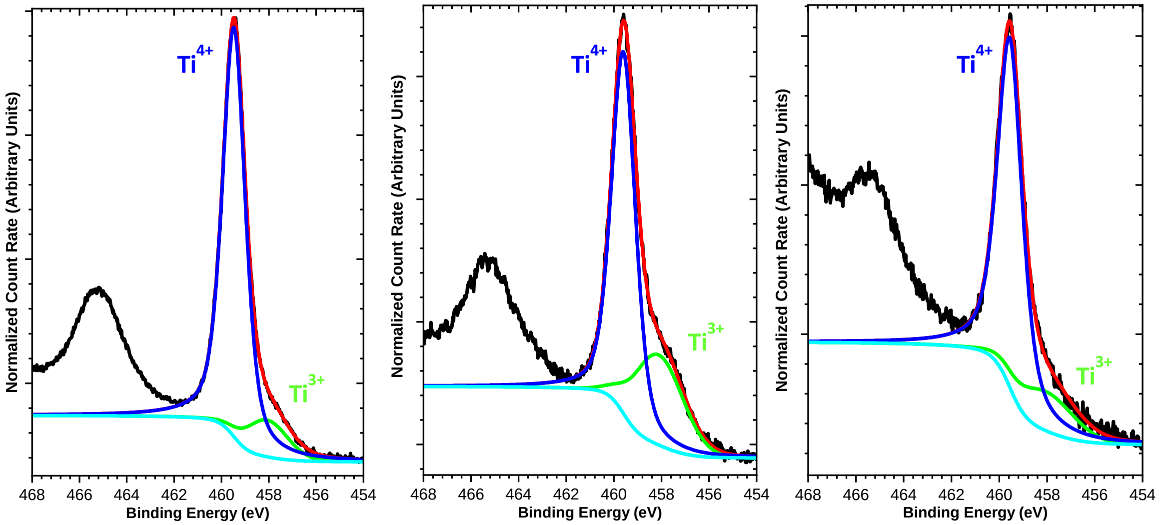
(a) 0 cycle surface (b) 8 cycles surface (c) 30 cycles surface

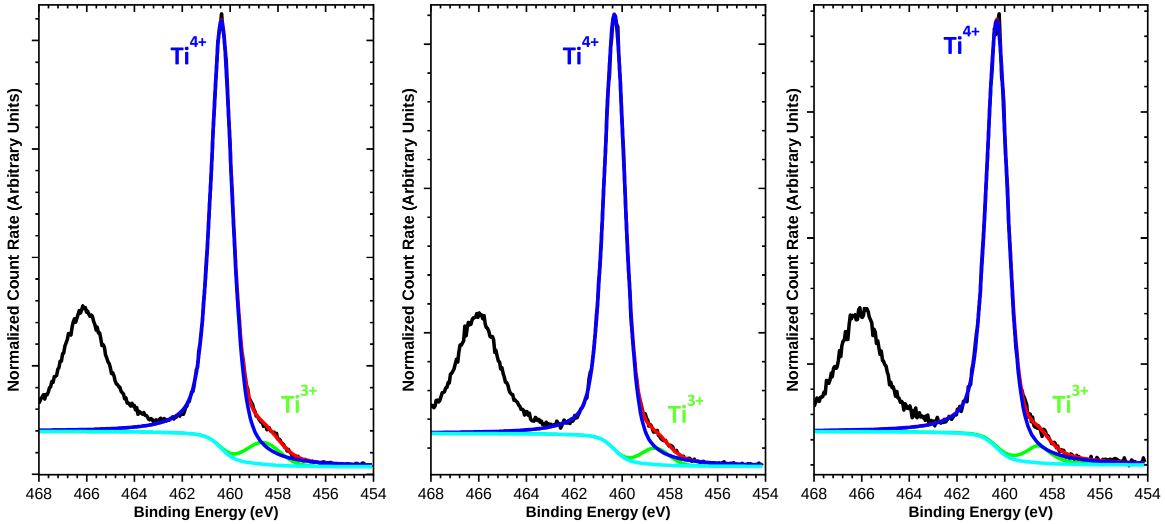
(d) 0 cycle bulk (e) 8 cycles bulk (f) 30 cycles bulk

Figure 11. Surface (top) and bulk (bottom) sensitive XPS measurements and deconvolution analyses of Ti 2p core level. The Ti 2p spectra were deconvoluted into two peaks: Ti^{3+} and Ti^{4+}.

(a) 0 cycle surface (b) 8 cycles surface (c) 30 cycles surface

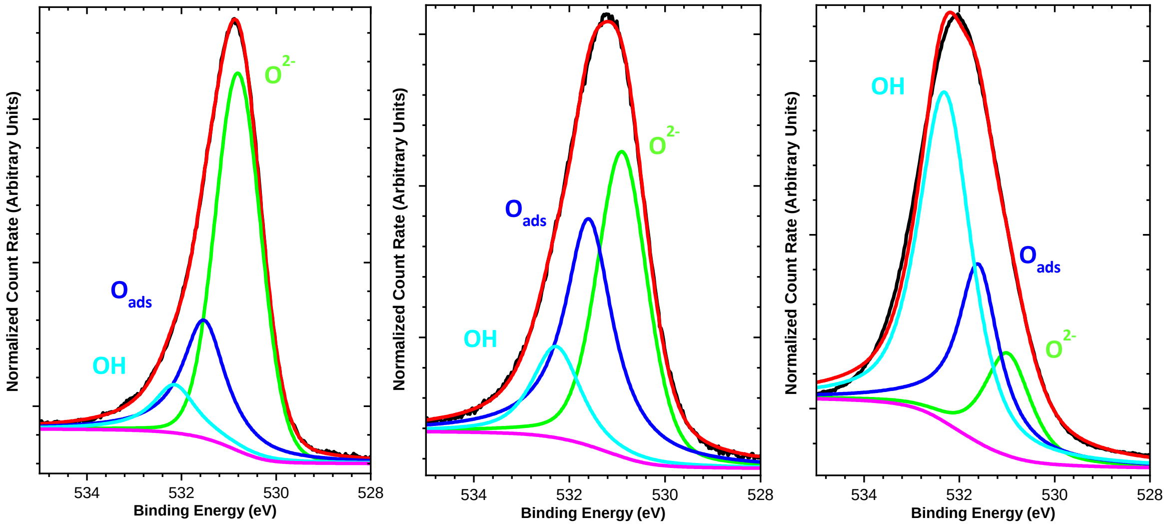

(d) 0 cycle bulk (e) 8 cycles bulk (f) 30 cycles bulk

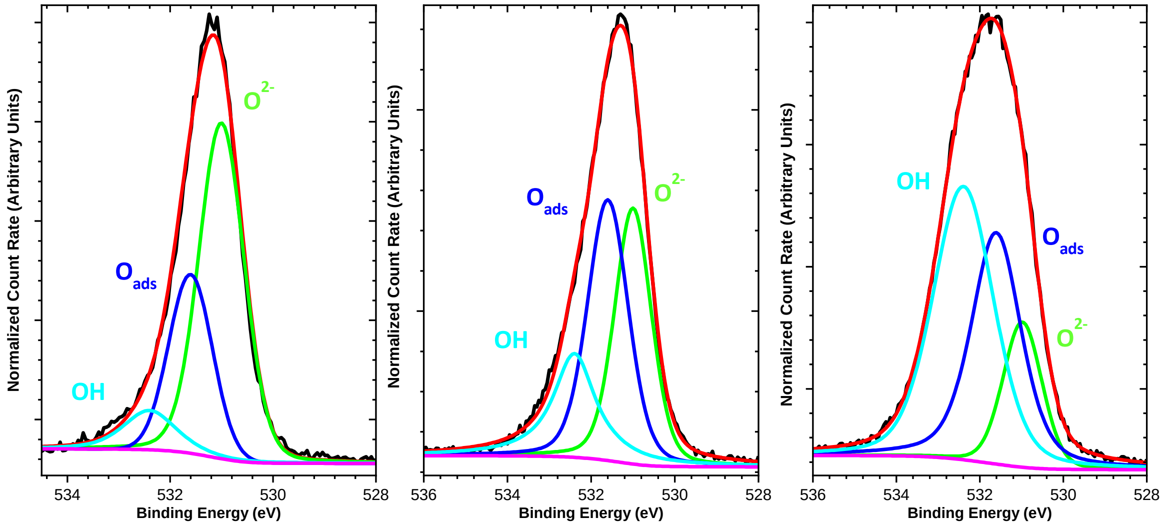

Figure 12. Surface (top) and bulk (bottom) sensitive XPS measurements and deconvolution analyses of O 1s core level. The O 1s spectra were deconvoluted into three peaks: lattice oxygen (O^{2-}), adsorbed oxygen (O_{ads}), and hydroxyl groups (OH).

(a) 8 cycles surface (b) 30 cycles surface

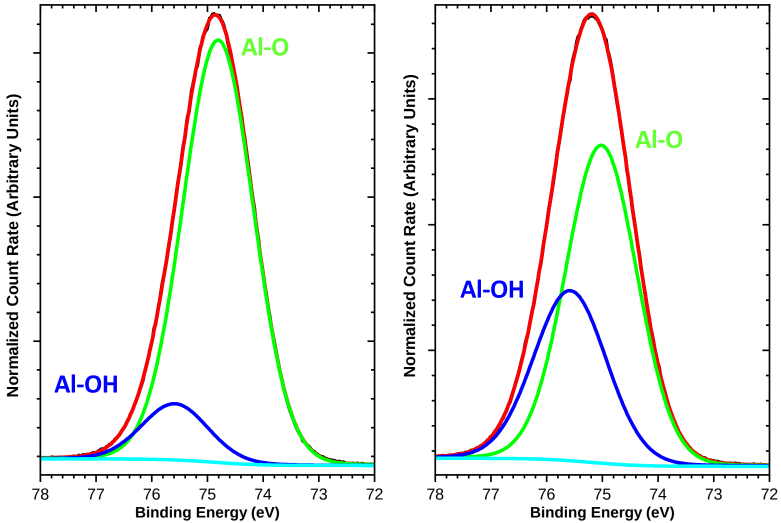

(c) 8 cycles bulk (d) 30 cycles bulk

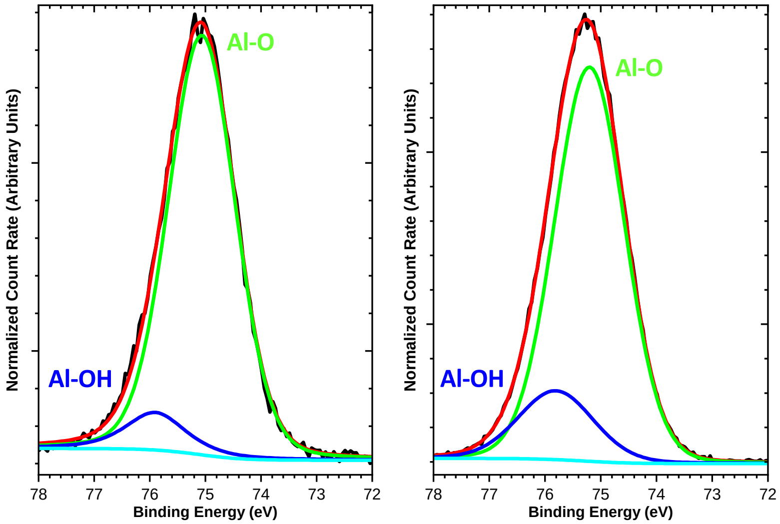

Figure 13. Surface (top) and bulk (bottom) sensitive XPS measurements and deconvolution analyses of Al 2p core level. The Al 2p spectra were deconvoluted into two peaks: Al-O and Al-OH bonds.

Lastly, the Al 2p XPS spectra were analyzed with peak fitting and deconvolution. In **Figure 13**, two peaks located at around 74.5 eV and 75.6 eV are assigned to Al-O and Al-OH bonds, respectively.[33] There is no other peak observed at a lower binding energy (i.e., 73 eV) to indicate the presence of Al-Al bonds; therefore, the Al is completely oxidized in the ALD process.[33] As seen in the O 1s spectra, the amount of hydroxyl groups was the greatest in the surface of 30 cycles (64%) compared to 8 cycles (17%). However, the difference was a lot smaller in the bulk, suggesting that most of Al-OH bonds were formed on the surface by the ALD surface-saturation reactions. There exists some small discrepancy between surface and bulk sensitive XPS measurements in terms of Ti 2p, O 1s, and Al 2p peak positions, suggesting that the growth conditions might have been consistent during the ALD process. For future works, it is important to control the ALD growth conditions so that the XPS profile would not change at different depth levels.

The Ti L-edge XAS spectra (**Figure 14**) confirmed the presence of Ti^{3+} on TiO_2 conforming to the XPS analyses. The spectra demonstrate that the core electrons from the Ti $2p_{3/2}$ and $2p_{1/2}$ states fill the vacant 3d orbitals.[34] The electronic transition gave rise to two significant features in the XAS spectra: Peaks a, b, A, B, and C in **Figure 14** when the 3d orbitals were occupied with electrons from the $2p_{3/2}$, and Peaks D and E when occupied with those from the $2p_{1/2}$.[34] Specifically, Peak A centered at around 458.5 eV was resulted from the electronic transition from the Ti^{4+} ground state (i.e., $3d^0$) to t_{2g} orbital (i.e., $3d_{t_{2g}}$), one of the degenerate orbitals in the Ti 3d band. On the other hand, the t_{2g} orbital was already occupied with an electron in the reduced Ti state of Ti^{3+}, potentially decreasing the number of 3d unoccupied states. Considering the XAS spectral configuration as a linear combination of Ti^{3+} and Ti^{4+} contributions, the transfer of spectral weight from Ti^{4+} to Ti^{3+} peaks would result in reducing the relative intensities of Peaks a, b, and A and strengthening the relative intensity of the dip between Peaks A and B.[35,36] These features originating from the Ti^{3+} contribution are most noticeable in the XAS spectrum of black TiO_2 nanotube arrays with 8 cycles, thereby verifying the presence of Ti^{3+} and indicating its highest concentration in agreement with the XPS results.

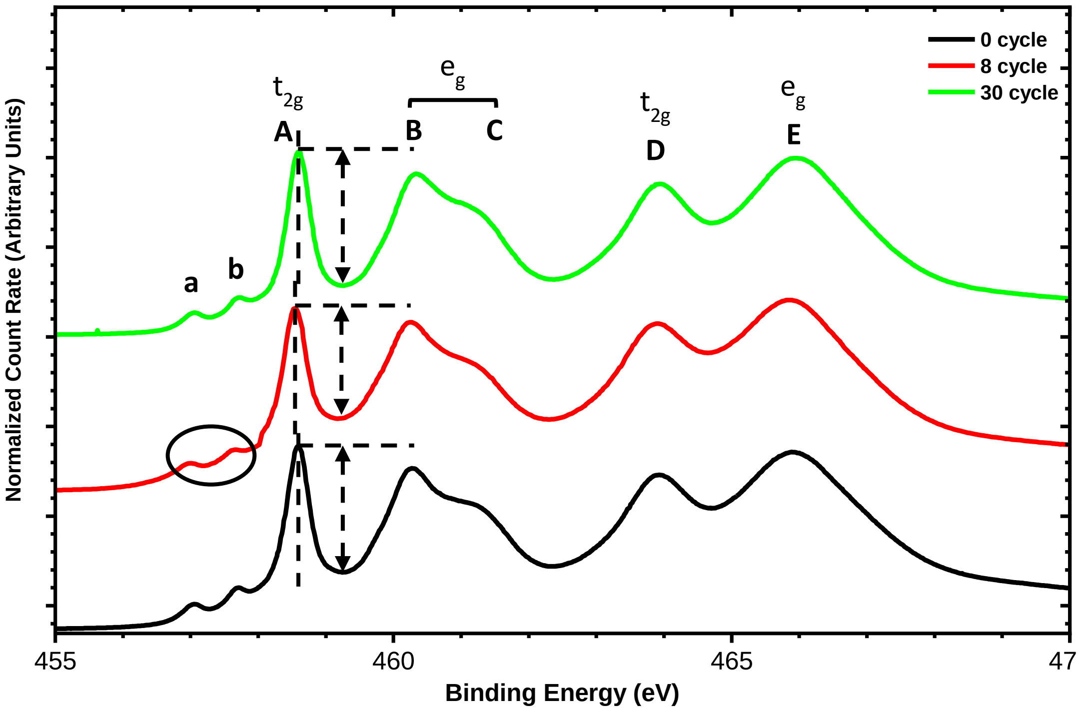

Figure 14. Ti L-edge XPS spectra of black TiO_2 nanotube arrays with 0 cycle, 8 cycles, and 30 cycles.

The deposition of ultrathin Al_2O_3 overlayer enhanced the bulk conductivity of black TiO_2 nanotube arrays by introducing the Ti^{3+} and oxygen vacancy pairs into TiO_2 lattice. Ti^{3+} and oxygen vacancies were formed on the TiO_2 surface and bulk by the ALD process, as well as hydrothermal treatment. During the Al_2O_3 overlayer deposition, TMA, a strong reducing reagent, reduced the surface and subsurface of TiO_2 nanotube networks, consequently generating the reduced Ti state and oxygen vacancies.[37] 0 Furthermore, the catalytic activities of black TiO_2 nanotube arrays were improved with Al_2O_3 ALD, resulted from a higher number of active sites. Particularly, oxygen vacancies on the surface are regarded as active sites for the OER.[38] Therefore, the highest catalytic activity for the OER was observed with 8 ALD cycles that contained the most abundant surficial oxygen vacancies in accordance with the ECSA and XPS results.

Black TiO_2 nanotube arrays with 8 ALD cycles of Al_2O_3, which demonstrated the highest CER performance, tested in comparison to a commercial IrO_2 DSA for the treatment of toilet wastewater from the pilot scale toilet system installed at Caltech. Toilet wastewater contains chloride ion (30 mM) from urine that can be oxidized to reactive chlorine species (RCS) (e.g., Cl_2) via the CER.[39] Subsequently, electrochemically produced RCS degrades organic and inorganic contaminants, and the degradation efficiency can be estimated by measuring COD and NH_4^+ levels, respectively, for example. As shown in **Figure 15 (b) and (c)**, black TiO_2 nanotube arrays with 8 cycles outperformed the IrO_2 DSA in both COD and NH_4^+ reductions, confirming their higher CER activity. After 5-hour electrochemical treatment, the substrate with 8 ALD cycles produced a visually transparent effluent very distinguishable from raw toilet wastewater (**Figure 15 (d)**). In addition, the production of hydroxyl radical, one of reactive oxygen species, was evaluated for both substrates. Black TiO_2 nanotube arrays with 8 cycles showed higher a higher production rate of hydroxyl radical by more effectively degrading the probe molecule (i.e., BA). The produced hydroxyl radical as well as RCS participated in COD reduction, justifying the superior degradation efficiency of the substrate with 8 cycles. Further research can be conducted to characterize the effluent quality more in detail and determine its viability for non-potable and/or potable water applications.

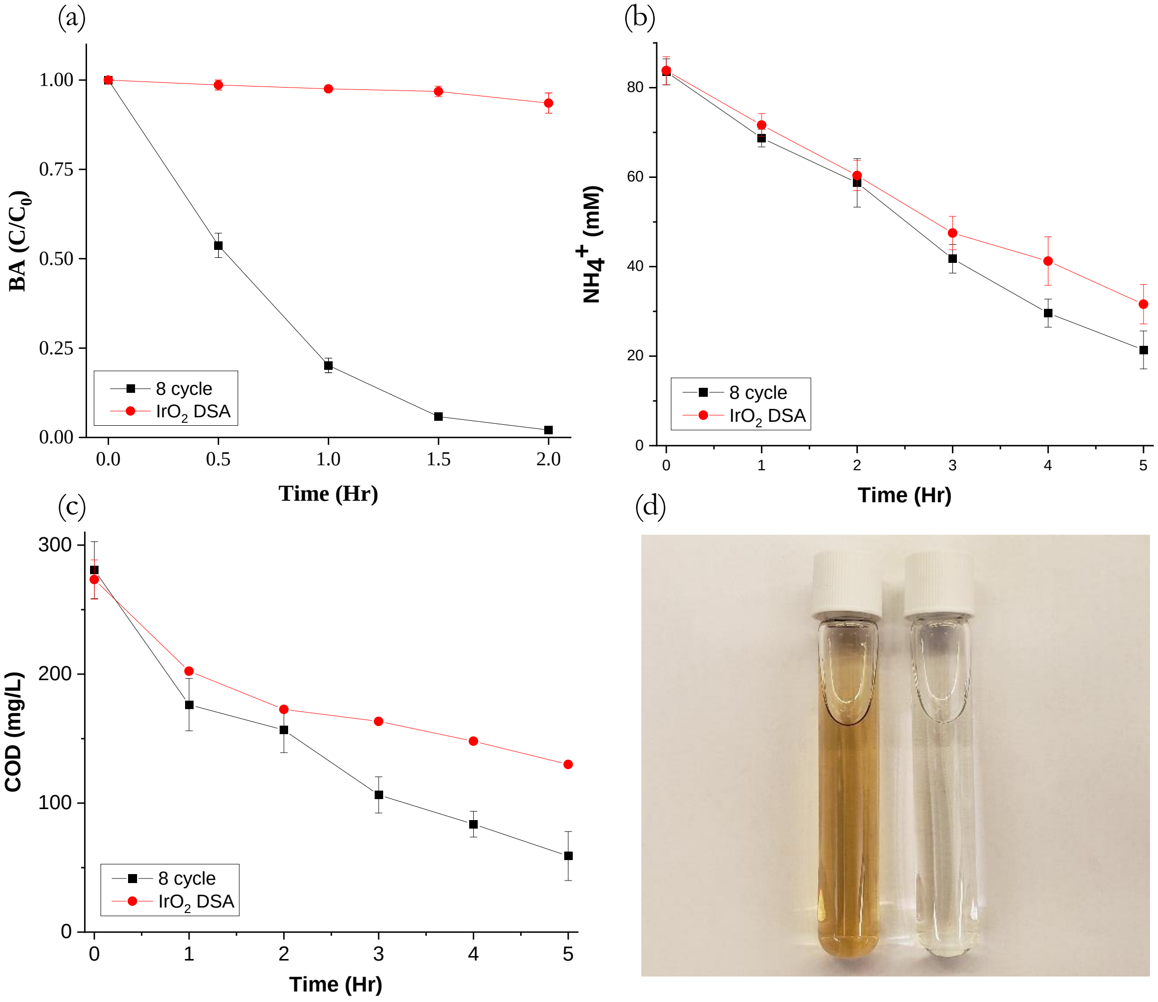

Figure 15. Treatment performance comparison between black TiO_2 nanotube arrays with 8 cycles and IrO_2 DSA in terms of (a) BA, (b) NH_4^+, and (c) COD reduction. (d) Comparison between raw toilet wastewater (left) and treated wastewater (right) after 5-hour electrolysis by black TiO_2 nanotube arrays with 8 cycles.

2.4. Conclusion

In summary, black TiO_2 nanotube arrays were deposited with ultrathin Al_2O_3 overlayer via ALD, and 8 ALD cycles that were most abundant with Ti^{3+} and oxygen vacancies demonstrated superior conductivity and significant improvements in CER and OER catalytic activities compared to those without Al_2O_3 ALD. Not only did 8 cycles show the highest CER and OER current densities that were normalized to geometric surface area and ECSA, but they also achieved the lowest overpotentials for the reactions at the geometric current densities of 1 mA/cm^2 and 10 mA/cm^2. Furthermore, CER and OER ECSAs were enlarged with ultrathin Al_2O_3 coating three times greater than bare black TiO_2 nanotube arrays. Characterization confirmed that the outstanding electrocatalytic performance of 8 ALD cycles could be ascribed to the abundance of Ti^{3+} and oxygen vacancies, which could considerably increase bulk conductivity and the number of electrochemical active sites. We believe this facile Al_2O_3 ALD synthesis strategy will be of great use for fabricating highly effective, practical electrocatalysts for a variety of energy and environmental applications. However, there are some remaining works to be conducted to put this novel electrocatalyst system into application. The long-term stability of black TiO_2 nanotube arrays should be examined with Al_2O_3 ALD, one of the significant prerequisites for electrocatalysts. Moreover, more morphological characterization will be needed by evaluating the uniformity and conformity of Al_2O_3 ALD on the TiO_2 nanotube networks via atomic force microscopy (AFM) and inspecting the cross sections to ensure the deposition on the nanotube inner walls. Lastly, the crystal structures of black TiO_2 nanotube arrays with and without Al_2O_3 ALD should be determined by X-ray diffraction analysis (XRD).

CHAPTER 3: Onsite Graywater Treatment in a Two-Staged Electro-Peroxone Reactor with a Partial Recycle of Treated Effluent

3.1. Introduction

Climate change has increased water scarcity in many parts of the world leading to the need for development of new practices for water supply management.[1, 2] Onsite water reuse is one of the key opportunities to increase water supply without a detrimental impact on the environment.[3] Important steps in this direction have been taken through the development of non-sewered sanitation systems with low- or near-zero water consumption competing with large scale wastewater treatment plants.[4, 5] A complementary approach is the treatment and reuse of graywater. This new paradigm provides a steady water supply that is not influenced by seasonal availability or need.[6] Furthermore, the level of desired treatment can range from treating graywater for reuse in low contact systems (e.g., as flushing water) or as a first-step treatment to convert processed water into potable water.[1, 2]

In order to achieve a high-level of water quality for reuse as described in the recommended NSF 350 standard,[7] graywater treatment systems often employ the same processes as used in large-scale wastewater treatment plants. In general, the treatment train starts either with primary sedimentation or multi-media filtration; these steps are then followed by fixed-bed biological treatment and chemical disinfection.[8] Even though this approach has proven to be effective, the biological treatment requires a residence time ranging from 5 to 24 hours[9] in a large-volume bioreactor. Advanced graywater treatment systems capable of reducing the organic load and disinfecting the product water without biological treatment may allow for a much smaller footprint for a household graywater recycling system.

Advanced oxidation processes (AOPs)) primarily rely on in situ generation of hydroxyl radical (·OH) as the primary oxidant due to its very high reduction potential and related reactivity as a one-electron oxidant of susceptible organic and inorganic electron donors ($E°(\cdot OH/H_2O)$ = 2.80 V *vs.* SHE). Physico-chemical methods for hydroxyl radical

This chapter was reprinted with permission from *ACS EST Engg.* 2021, 1, 12, 1659–1667.

production including ultrasonic radiation or sonolytic ozonation,[10] UV/H_2O_2 and UV/O_3 photolysis, or utilizing the O_3/H_2O_2 peroxone reaction.[11] However, these methods are limited by their operational costs. In the case of hydrogen peroxide, storage of high concentrations (e.g., ≥30% by weight of H_2O_2) requires special hazardous chemical precautions. Hydrogen peroxide is susceptible to autocatalytic decomposition into oxygen and water, which may lead to an explosion in an unvented storage container.

To avoid the high cost of H_2O_2, the electro-peroxone process (E-peroxone) can be used to produce H_2O_2 onsite via the electrochemical reduction of oxygen. Since both ozone and H_2O_2 are generated with oxygen, onsite generation of both oxidants' problems associated with reagent storage are avoided.

Combining electrochemical H_2O_2 production using carbon cathodes coupled with O_3 also generated onsite in a single reactor has been investigated by Wang,[12] but the short lifetimes of carbon cathode in the presence of ·OH makes the single reactor approach challenging for practical applications. This is particularly true for small-scale treatment of wastewater in onsite, semi-autonomous units where component replacement should be minimized.[13] In comparison to the single-step E-peroxone process, H_2O_2 production is separated from the actual peroxone reaction chamber in order to increase the lifetime of the carbon cathodes from attack by ·OH. The quality of the effluent from the dual-chamber reaction system is designed to be suitable for either discharge, recycling as toilet flushing water, or returning into the H_2O_2 production chamber as source water. The system as tested is shown to be suitable for either a single-pass treatment sequence or for the continuous reuse of treated graywater as influent for the H_2O_2 generation step. The goals of the reaction system are to meet the requirements of the standards established by NSF 350/350-for effluent quality terms of COD, TOC, BOD, pH, and turbidity for either the safe discharge into receiving waters or for reuse for non-potable water applications such as toilet and urinal flushing.

3.2. System Design

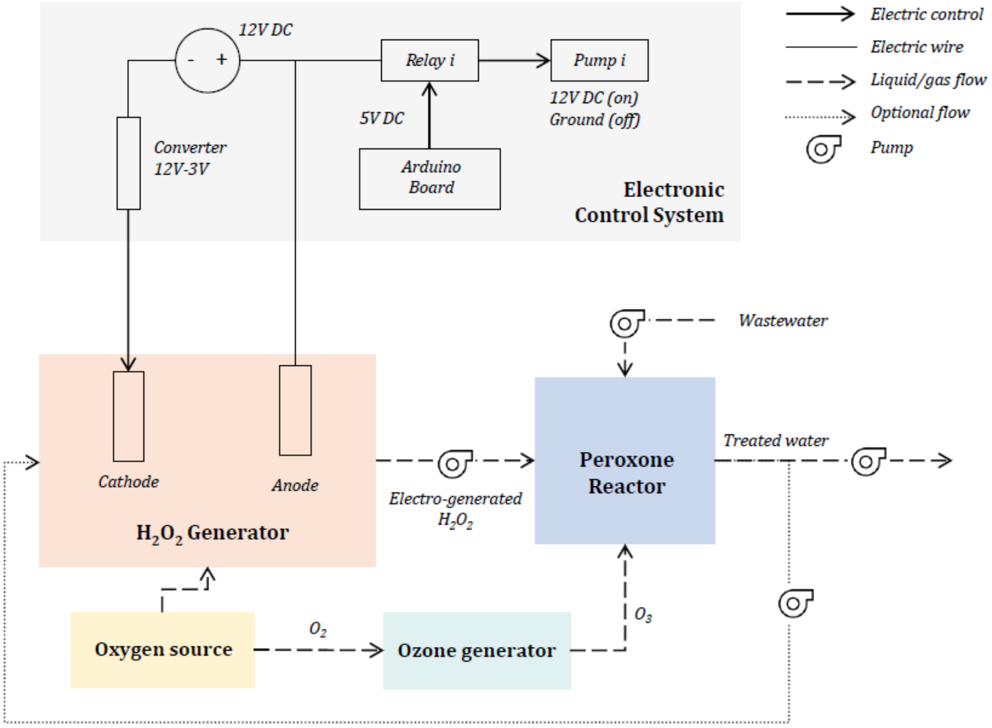

Figure 1. Schematic diagram of an integrated electro-peroxone reactor system. A single power supply provides the applied potential power the electrolysis and to run the mechanical components needed for a continuous-flow reaction system.

3.2.1 Overall Design

The electro-peroxone system developed in this study consists of two separate chambers as shown in **Figure 1**. The first chamber is an electrochemical H_2O_2 generator, and the second chamber is the reactor the peroxone reaction leading to ·OH production. A laboratory-scale prototype shown in **Figure S1** (Supplementary Information). The two chambers are connected using flexible silicone tubing (5 mm ID × 7 mm OD, Uxcell, Hong Kong, China) to transfer the electrochemically generated H_2O_2 from the first reactor to the peroxone reactor using a peristaltic pump (INTLLAB, Shenzhen Jiashi Technology Co. Ltd., Shenzhen, China). Influent water (e.g., synthetic graywater) is pumped into the peroxone reactor, where it was combined with O_3 and electrochemically generated H_2O_2. Finally, the treated water is either collected or recycled for use in the following cycle of treatment. Both chambers have collection ports for sampling.

3.2.2. Electrochemical H_2O_2 Generation

The H_2O_2 generator is a custom-designed 500-mL reactor made from ABS-based plastic (VisiJet Armor (M2G-CL) (MJP)) that is 3D-printed using a ProJet MJP 2500 Plus (3D SYSTEMS, Rock Hill, SC). A titanium O_2-diffuser is place along the center line and at the bottom of the reactor at a flow rate of 0.8 standard cubic feet per hour (SCFH). The electrode pair is placed above the O_2-diffuser in a 3D-printed 110 mm × 70 mm × 105 mm ABS-based housing, which covers the edges of the electrodes to prevent electrical shortages and to increase the mechanical stability of the electrolysis unit (**Figure S2**, Supplementary Information). The electrolysis cell consists of three polytetrafluoroethylene (PTFE)-coated carbon cathodes (CP75T carbon fiber paper, AVCARB MATERIAL SOLUTIONS, Lowell, MA) placed in a sandwich configuration between two IrTaO-TiO_x anodes (Nanopac, Korea). A constant electrical potential of +3 V is applied between the cathodes and the anodes during H_2O_2 electrolysis. 50 mM Na_2SO_4 (Macron Fine Chemicals, Center Valley, PA) in deionized water (Milli-Q, Millipore) is initially used as the electrolyte. In the subsequent treatment cycles, treated graywater is used as the electrolyte.

3.2.3. Peroxone Reactor

The peroxone reactor is a customized 1-L cylinder with two liquid ports and one gas infuser. The influent (i.e., synthetic graywater) is added directly from an external waste container, while H_2O_2 is transferred from the H_2O_2 generator and introduced at the bottom of the peroxone reactor using a flexible tubing. An external O_3 generator (CNC6390-1V, Eleoption) with an average power consumption of 65 W is used to convert oxygen to O_3 with a 5% efficiency, delivering 71.5 mg/L of O_3 to the peroxone reactor during the cycle treatment. The O_2/O_3 diffuser at 0.8 SCFH was placed slightly above the bottom of the reactor. Mixing in the reactor is achieved by the turbulence generated by the flow of O_2/O_3. Treated wastewater is pumped out from the bottom of the cylinder to an external storage container.

3.2.4. Electronic and Pumps

The entire system is powered by a 12V DC, 0-30 A power supply (Supermight). The output voltage is converted to 3V using an adjustable DC-DC converter (DROK LM2596) to drive the H_2O_2 generator. The output voltage is continuously monitored and displayed using a MCIGICM 0.28" LED Voltmeter Ammeter.

Liquid flow in the system is controlled by five identical INTLLAB peristaltic pumps 3 mm ID x 5 mm OD, powered by the 12V DC, 0-30 A power supply. The flow from each pump is controlled at 100 mL/min by five YOUNGNEER 5V Relays controlled by an ARDUINO UNO R3 board.

3.3. Methods

3.3.1. Treatment Sequence

The system described in Section 3.2 was used in all the treatment tests presented in this study. A full test sequence started with H_2O_2 generation using 0.8 SCFH of O_2 and 3 V of applied potential at the electrodes of the H_2O_2 generator. The H_2O_2 generation step lasted until the desired concentration of H_2O_2 (~2.25 abs or 4.8 mM) was reached (between 60 to 90 minutes). A 250 mL solution of the electrochemically generated H_2O_2 was introduced in to the peroxone reactor in three injections of equal volume each at 0, 10, and 20 minutes, unless noted otherwise. O_2 was converted to O_3 by the O_3 generator and continuously introduced into the peroxone reactor at 0.8 SCFH until the end of treatment. Aliquots of graywater were collected for chemical and physical analysis every 10 minutes for the first 60 minutes of treatment and lastly at the end of the treatment at 90 min.

3.3.2. Consecutive Runs

The first treatment sequence was conducted using 50 mM Na_2SO_4 electrolyte in 500 mL DI water for H_2O_2 generation. Treated graywater was used as the subsequent electrolyte for the following treatment cycles. In this case, 440 mL of the treated graywater were added back into the H_2O_2 reactor before electrolytic H_2O_2 generation. The submerged electrode surface area was kept constant in the H_2O_2 chamber. Two 20-mL glass vials were immersed in the chamber to compensate for the volume loss caused by sampling during treatment. The duration of the electrolysis of H_2O_2 was adapted to reach a concentration of ~4.8 mM H_2O_2. Following the generation of H_2O_2 all consecutive steps were identical to the full system treatment sequence as described in Section 3. This process was repeated until the fourth treatment sequence was achieved. The reactor and associated tubing were flushed with 500 mL of DI water between each run.

3.3.3. Cyclic Voltammetry

Cyclic voltammetry (CV) was performed in a 50 mM Na_2SO_4 solution in a four-necked flask, employing a three-electrode configuration that was connected to a Bio-Logic VSP-300 Potentiostat (Seyssinet-Pariset, France). The working electrode was a 1 cm × 1 cm PTFE-coated carbon paper electrode exposed on a single side and covered on the backside with epoxy. A CHI 151 $Hg/HgSO_4$ electrode (CH Instruments, Austin TX, USA) was used as the reference electrode, while a platinum counter electrode and an outlet for gases occupied the third neck of the flask. The fourth neck was used as an inlet for nitrogen (N_2) or oxygen (O_2) gas purging. N_2 or O_2 was purged into the flask for saturation for 30 minutes before CV and then constantly purged throughout the CV scans. Either gas was bubbled through another 50 mM Na_2SO_4 solution before introduction to the flask to reduce evaporation. CV was performed at scan rate of 10 mV/s in the potential range of –1.0 to 0.0 V.

3.3.4. Cathode Materials

The H_2O_2 production rates over 60 minutes using different carbon-based materials were determined (**Table S1**, Supplementary Information). Chemical compatibility and cost of materials were also considered. Each cathode material had the same surface area (8 cm^2) in contact with 400 mL of a solution of Na_2SO_4 at 50 mM. The anode was a composite IrTaO-TiO_x electrode (Nanopac, Korea). Oxygen was supplied at constant flow rate of 1.7 SCFH.

3.3.5. Sample Collection and Characterization

10-mL samples were collected 10 cm from the bottom of the peroxone reactor using a 25-mL pipette and were briefly stored at room temperature (21 ± 1 °C) before being analyzed for turbidity, [H_2O_2], COD, pH, and TOC. Unless noted otherwise, the measurements were performed in triplicates.

Turbidity: Turbidity was measured using the HI93414 Turbidity meter (Hanna Instruments, Woonsocket, USA) following the method recommended by the manufacturer.

[H_2O_2]: A 0.5-mL sample was combined with an equal volume of a titanium oxalate solution as per Sellers, 1980.[14] The 407-nm absorbance of the resulting mix was measured by UV-Vis spectroscopy using a Nanodrop 2000c spectrophotometer (Thermo Scientific, Waltham, USA). The system was blanked with Milli-Q water beforehand.

Chemical Oxygen Demand (COD): After appropriate dilution, COD was measured by colorimetry following Hach Method 8000 with low-range 3-150 mg O_2/L COD vials and a DR 900 Colorimeter (Hach, Loveland, USA).

pH: pH was determined using an Orion Star A215 pH/conductivity meter (Thermo Scientific, Waltham, USA) connected to an Orion 8157BNUMD Ross Ultra pH/ATC Triode (Thermo Scientific, Waltham, USA).

Total Organic Carbon (TOC) and Total Inorganic Carbon (TIC): In addition to COD measurements, the TOC and TIC concentrations in the synthetic graywater samples were measured over the course of treatment using a TOC analyzer (OI Analytical Model 1030W, College Station, TX). The TOC content was obtained indirectly by subtracting the measured TIC content from the measured total carbon (TC) content. While TIC was quantified in the gas produced by phosphoric acid (5% v/v, Fisher Scientific, Hampton, NH) treatment, TC was quantified by oxidation of all the existing carbon in the sample with $Na_2S_2O_8$ (10% w/v, Acros Organics, Fair Lawn, NJ).[15] The sample was diluted at 1:4 ratio with Milli-Q water prior to analysis, except for the last extract obtained at 90 minutes due to its very low TOC content.

Total Nitrogen (TN) and Total Phosphorus (TP): TN and TP of the synthetic graywater were determined by colorimetry using a Hach DR 900 colorimeter (Hach, Loveland, USA) at the beginning and at the end of the treatment. For the TN measurement, Hach Method 10071 was used with Test ‘N Tube Low Range Total Nitrogen Reagent Set. For the TP measurement, Hach method 8190 was used with Test ‘N Tube Low Range Total Phosphate Reagent Set.

Biochemical Oxygen Demand (BOD): BOD was measured after a 5-day incubation period following Standard Method 5210B[16] using an Accumet XL40 Dissolved Oxygen Meter (Fisher Scientific, Waltham, MA) connected to an Orion BOD probe (Thermo Scientific, Waltham, MA). The samples collected after treatment (90 minutes) were bubbled with air for approximately 5 minutes after dilution and prior to measuring the dissolved oxygen.

3.3.6. Graywater Synthesis

The synthetic graywater used in this study (**Table S2**, Supplementary Information) was adapted from the NSF 350/350-1 standard.[17] A 10-L batch of synthetic graywater was prepared in a 30-L container by dissolving the components in tap water, except for deodorant and toothpaste. A premix solution of deodorant and toothpaste was prepared separately in 450 mL of tap water at 65 °C and mixed at 700 rpm for 20 minutes, and then added to the container. Finally, the synthetic graywater solution was mixed with a DLH overhead stirrer (Velp Scientifica, Usmate, Italy) at 2,000 rpm for 20 minutes and settled for 10 minutes before use. Synthetic graywater from the same batch was used for each consecutive testing. The graywater was characterized and found to be consistently within the range of water matrices described in the NSF 350/350-1 standard (see **Table S3**, Supplementary Information).

3.4. Results and Discussion

3.4.1. Single Run Testing

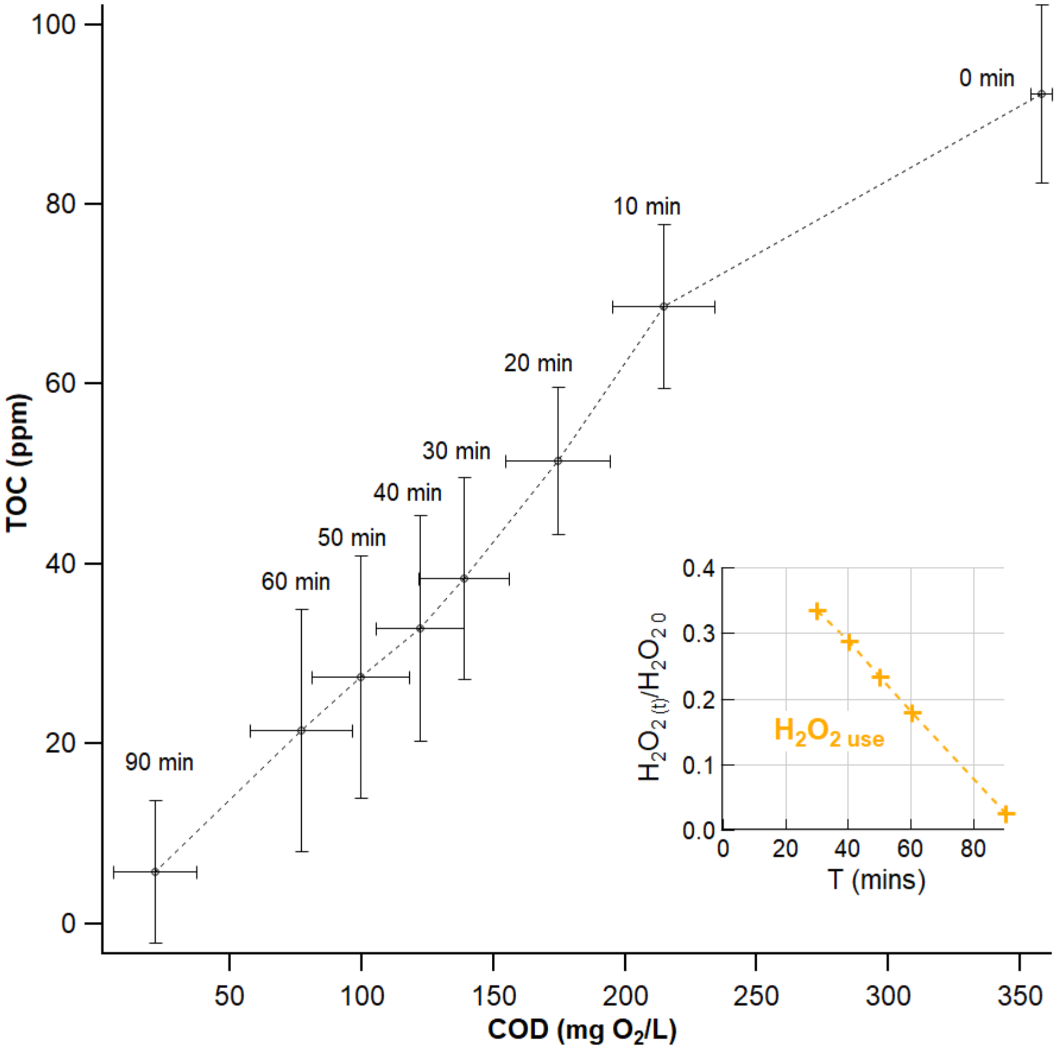

Figure 2. Co-evolution of TOC and COD concentrations in the peroxone reactor. Electrochemically generated H_2O_2 was added to the reactor in equal volumes after 0 minute, 10 minutes, and 20 minutes of E-peroxone treatment. (Inset: concomitant evolution of [H_2O_2] in the peroxone reactor during treatment.) Error bars represent ± standard deviation from the mean.

A decrease in COD and TOC concentrations in the bulk solution of the peroxone reactor was observed during each run (**Figure**) following the treatment sequence described in Section 3.3.1. Graywater had an average initial COD level of 358.5 ± 3.8 mg O_2/L and reached a COD level of 21.25 ± 15.70 mg O_2/L at the end of the 90-minute treatment run. The average percent COD removal was 94% in solution and 89% when adjusted for dilution. In addition to observing COD removal, the TOC of the solution was degraded by 92% (86% adjusted for dilution) during the E-peroxone process with starting TOC concentrations of 96.95 ± 9.84 ppm and final TOC concentrations of 7.29 ± 7.86 ppm. As a comparison, conventional ozonation was performed by substituting H_2O_2 with Milli-Q water added to the system in the same injection patterns (0-minute, 10-minute, and 20-minute), and we observed both COD and TOC removals of only 57% and 43%, respectively. The large difference between injection of H_2O_2 solution or Milli-Q water confirms that the E-peroxone treatment was more effective at oxidizing and mineralizing organics than ozonation alone.[11]

The decrease of COD and TOC concentration over time was not linear (**Figure 2**). COD and TOC decreased by an average of 34% and 27% during the first 10 minutes of the process while this removal was of approximately 19% and 20% during the next 10-minute increments, with limited effect of the injection of the electrochemically generated H_2O_2 solution. This difference between the initial rate and the rest can be attributed to the fact that there is a high concentration of organic species at the beginning of the treatment, leading to a higher removal efficacy. In addition, the fluctuation of the COD/TOC ratio (i.e., deviation from a constant) during the process was likely caused by organic matter not readily biodegradable or other recalcitrant organic contaminant in the solution.[18]

Finally, the removal efficacy observed for COD and TOC was upheld with regards to BOD elimination: the five-day BOD (BOD_5) decreased by 95% (91% adjusted for dilution) to reach on average 7.83 ± 6.49 mg O_2/L (14.32 mg O_2/L adjusted for dilution). The effluent met NSF350/350-1 Class R requirement for BOD_5 ($BOD_5 < 10$ mg/L).

The turbidity of synthetic graywater was initially 11.2 NTU. After 90 minutes of treatment (**Figure S3**, Supplementary Information), the turbidity decreased by 95%. Given that the graywater was mixed with the H_2O_2-containing Na_2SO_4 solution in equal volume during treatment, the observed turbidity reduction of graywater was partly caused by dilution. To evaluate the influence of dilution on the turbidity reduction, synthetic graywater was diluted with Milli-Q water at a 1:1 ratio with and without continuous oxygen flow through the peroxone reactor. In the 1:1 mixture of graywater and Milli-Q water, the turbidity decreased only by 42% with constant oxygen flow and by 47% without it. The small difference in turbidity reduction with and without oxygen can be attributed to the oxygen flow favoring the suspension of particles that were prone to adhere to the reactor wall. Conversely, the vast improvement in turbidity removal during the E-peroxone process correlated with high TOC and COD removal (vide supra) of this process. Small particles in suspension can be chemically oxidized and dissolve, as observed in agro-industrial wastewaters.[19] The results indicate that the E-peroxone process reduced the turbidity of graywater effectively enough to meet NSF 350/350-1 standard for both Class R (< 5 NTU) and Class C (2 < NTU).

pH remained stable (between 6.5 and 8) and met the NSF 350/350-1 standard ($6 < pH < 9$) range (**Figure S4**, Supplementary Information). On average, the pH decreased slowly from 7.8 to 7.0 during the first hour of treatment, most likely due to intermediate organic acid production in the system from peroxone-driven oxidation reactions.[5] However, the constant O_2/O_3 flow resulted in the stripping of newly generated CO_2 generated during mineralization of the organic constituents. Therefore, the pH rose to 7.3. A similar effect was observed by Cohen and co-workers.[20] The change in pH was reflected in an increase of TIC (i.e., carbonate alkalinity) during the last 30-minute of treatment, as shown in **Figure S5** of the Supplementary Information section.

The electrochemical peroxone process did not readily remove TN and TP in synthetic graywater at initial concentrations of 5.10 mg/L and 3.93 mg/L, respectively. Considering the dilution of the graywater with H_2O_2-containing Na_2SO_4 solution, TN nearly remained the same whereas TP decreased by 33% after 90-minute treatment. Moghadam et al. observed that the efficacy of phosphorus removal can be improved by favoring the peroxone reaction by increasing pH.[21] As a result, synthetic graywater can be adjusted with higher pH before treatment, as the kinetics of ·OH formation is enhanced in basic condition,[12] for more effective phosphorus removal. On the other hand, AOPs such as the E-peroxone process that based on ·OH as the primary oxidant are known to be ineffective for nitrogen removal. For example, ammonium ion/ammonia reacts with ·OH at much slower rates than oxidizable contaminants.[22] Therefore, integrating the E-peroxone process with an additional treatment step (e.g., ion exchange, activated carbon[23] or chlorination[24]) may lead to improvement of the nitrogen removal efficiency in the case of graywater. This integration would expand the scope of application of the E-peroxone process for treating human wastewater that has higher nitrogen loads.

3.4.2 Consecutive Testing

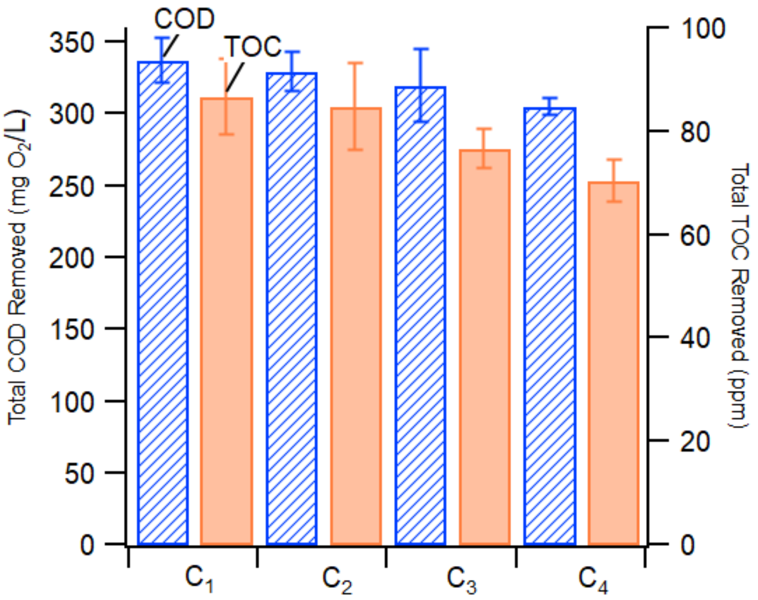

Figure 3. Average COD removal (COD_{rem}) and TOC removal (TOC_{rem}) from graywater during four consecutive treatment cycles (C_1 through C_4). Error bars represent ± standard deviation from the mean.

The COD removal (COD_{rem}) extent remained above 300 mg O_2/L for each 90-minute treatment run (**Figure**) with a small decline from 337.25 ± 15.17 mg O_2/L (C_1) to 305 ± 5.7 mg O_2/L (C_4). Similarly, TOC removal (TOC_{rem}) remained above 70 ppm for each 90-minute treatment run (**Figure 3**) but with a slightly more significant decline: from 86.63 ± 7.35 ppm (C_1) to 70.35 ± 4.2 ppm (C_4). Despite the decrease in TOC removal efficiency, the graywater quality standards were maintained for COD and TOC, even when the effluent was recycled into the H_2O_2 generator 4 times. The treatment performance declined faster after a fifth treatment cycle, potentially due to the decrease in electrolytic H_2O_2 production due to a stepwise reduction in conductivity (vide infra). The decline in COD_{rem} and TOC_{rem} over consecutive cycles can be explained by two main factors: (1) the impact of the recycled effluent and (2) the decrease in H_2O_2 production.

The COD_{rem} and TOC_{rem} decreases may also be due to the accumulation of organics in the system as the effluent from C_1 (Ef_1) was recycled for H_2O_2 electro-generation in C_2, the value of COD Ef_1 = 21.25 ± 15.71 mg O_2/L and TOC Ef_1 = 7.29 ± 7.86 mg O_2/L (the Na_2SO_4 electrolyte solution used in C_0 had no detectable amounts of COD or TOC). COD and TOC in Ef_1 did not degrade during the electro-generation of H_2O_2 (data not shown). As a result, COD and TOC values increased in C_2 compared to C_1 when the electro-generated H_2O_2 solution from Ef_1 was injected into the peroxone reactor. The same phenomenon was accentuated in the subsequent cycles (C_3 and C_4).

The second factor impacting COD_{rem} and TOC_{rem} decrease is due to the lower [H_2O_2] in the electro-generated solution that was injected into the peroxone reactor. This decrease is attributed to a loss of conductivity (vide infra). Because the peroxone reactor is saturated ·with O_3, H_2O_2 is the limiting reagent in the peroxone process. Consequently, the decrease of [H_2O_2] in the solution injected into the peroxone reactor leads to a decrease of the steady state [·OH], which in turn impacts the degradation of organic components.

3.4.3. Effects of Recycling Treated Graywater on Electrochemical H_2O_2 Generation

The amount of time required to obtain an adequate [H_2O_2] (i.e., 4.8 mM) increased for each consecutive treatment test as treated graywater was recycled from the previous cycle for use in the electrochemical H_2O_2 production reactor. The increase of H_2O_2 generation time over multiple cycles is attributed to the change in the chemical composition of the electrolyte solution (i.e., as treated graywater is recycled). First, the solution conductivity is drastically reduced as the original 50 mM Na_2SO_4 electrolyte solution at a conductivity of 8 mS/cm is mixed and diluted with graywater with a much lower conductivity of ~0.7 mS/cm to produce H_2O_2 in subsequent cycles. In addition, a fraction of H_2O_2 may be simultaneously consumed by the organic compounds remaining in treated graywater due to incomplete organic mineralization. However, if treated graywater contains a high concentrations of chloride, reactive chlorine species (RCS) including hypochlorous acid (HOCl) and hypochlorite ion will be produced at the anode[25] during the reductive electrochemical generation of H_2O_2 generation resulting in a counterproductive scavenge of the generated H_2O_2.[26]

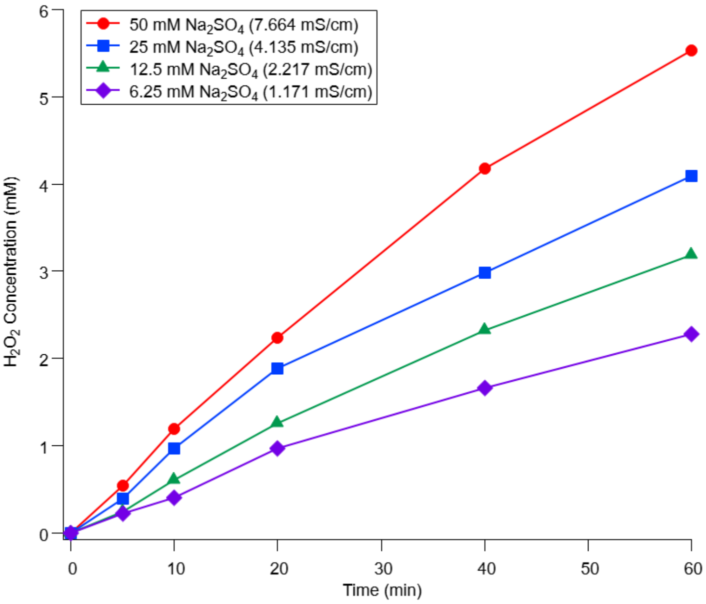

Figure 4. H_2O_2 generation in Na_2SO_4 electrolyte solutions at varying concentrations. H_2O_2 was generated for 60 minutes in the same setups as described in Section 3.2.2, except that a potentiostat was used to apply 3.00 V DC and measure the total electric charge for each electrolyte solution tested.

Table 1. Na_2SO_4 electrolyte concentration $[Na_2SO_4]_0$, conductivity, final $[H_2O_2]$ produced, total charge passed in each solution, and Faradaic Efficiency for H_2O_2 generation. The latter was calculated based on the final $[H_2O_2]$ and the total charge passed.

$[Na_2SO_4]_0$ (mM)	**50.0**	**25.0**	**12.5**	**6.25**
Conductivity (mS/cm)	7.664	4.135	2.217	1.171
Final $[H_2O_2]$ (mM)	5.529	4.091	3.187	2.278
Total charge passed (C)	812.14	612.36	475.34	314.51
Faradaic Efficiency (%)	65.69	64.46	64.69	64.89

To reproduce the decreasing conductivity observed over the course of consecutive tests, the original 50 mM Na_2SO_4 electrolyte solution was diluted with Milli-Q water at varying percentages: 50%, 25%, and 12.5%. Therefore, the electrolyte conductivity decreased proportionally by the dilution factors as shown in **Table 1**. Isolating the conductivity as a primary variable eliminates the potential impacts of residual organics in recycled treated graywater and of RCS formation on the net production of H_2O_2. **Figure 4** shows a decrease in H_2O_2 production due to decreasing conductivity in proportion to the actual Na_2SO_4 concentration. Lower electrolyte solution conductivity also increases the potential drop between the anode and the cathode in solution, thereby decreasing the total charge passed in the system as each test was run at a constant voltage. The Faradaic Efficiency of each run was calculated based on the total moles of H_2O_2 generated and the total charge passed during the 60-minute electrolyses. **Table 1** shows that the Faradaic Efficiency, which is proportional to the total moles of H_2O_2 produced and the inverse of total charge passed, remained unchanged regardless of the electrolyte conductivity. The constant Faradaic Efficiency indicates that other factors such as electrocatalytic activity loss and parasitic side reactions[27, 28] were not present to suppress the H_2O_2 generation efficiency. Therefore, the electrolyte conductivity, which was reduced during the reuse of treated graywater as influent to the first-stage reactor, was the primary factor increasing the extended time required to produce the same concentration of H_2O_2.

H_2O_2 has a high reduction potential of $E^o = 1.76$ V, although less than as O_3 ($E^o = 2.05$ V) and or hydroxyl radical ($E^o = 2.85$ V), which makes it a viable oxidizing agent for organic carbon in wastewater especially when activated (e.g., UV radiation, the Fenton reaction, or by peroxidases). If the concentrations of oxidizable organic compounds in the treated graywater are high enough, then H_2O_2 produced in the first reactor may be consumed by the remaining organics thereby increasing the time to achieve the target concentration of H_2O_2. As expected, mixing untreated graywater at 1:1 volume ratio with a clean electrolyte solution, the concentration of H_2O_2, which was 4.8 mM at time = 0, decreased by 40% after 1 hr of contact time (**Figure 4**). On the other hand, the loss of H_2O_2 was negligible in a mixture of treated graywater containing very low levels of oxidizable species after treatment with $\cdot OH$ and O_3 in the Peroxone Chamber.

If chloride is present in the influent to the first reactor, then $HOCl/^{-}OCl$ (i.e., RCS) would be produced at the anode, while H_2O_2 is generated at the carbon cathode. The formation of HOCl leads to direct scavenging of H_2O as follows:

$$HOCl + H_2O_2 \rightarrow H^+ + Cl^- + H_2O + O_2,\ k_2 = 1.10 \times 10^4\ M^{-1}s^{-1})^{26}$$

For example, combining H_2O_2 and HOCl in an equimolar molar ratio with initial concentrations of 4.8 mM, the concentration of H_2O_2 decreased by 30% after one hour. However, analysis by ion chromatography (data not shown) confirmed that the concentration of chloride (< 1 mM) in graywater was too low to produce a significant amount of HOCl during electrochemical H_2O_2 generation. The reaction of H_2O_2 and HOCl, however, may play a more significant role during electrochemical H_2O_2 generation for recycled waters with higher concentrations of chloride (e.g., toilet wastewater or brackish water).

3.4.4. Dosage of H_2O_2 into the Peroxone Reactor

The dosage of H_2O_2 was determined based on the H_2O_2 depletion rate observed in the peroxone reactor. Excess H_2O_2 in the second-stage reactor will react with in situ $\cdot OH$:[29]

$$\cdot OH + H_2O_2 \rightarrow HO_2\cdot + H_2O,\ \ k_2 = 2.70 \times 10^7\ M^{-1}s^{-1}.^{30}$$

Therefore, the rate of H_2O_2 transfer from the first-stage reactor to the peroxone reactor is optimized such that ·OH reacts with the target organic molecules in graywater without being scavenged by unreacted H_2O_2. To maximize the use of H_2O_2 for the generation of ·OH, 250 mL of the electrochemically generated H_2O_2 solution were injected into the peroxone reactor in three time-separated increments during the treatment. Each 83-mL volume of the H_2O_2 solution was injected at the beginning of the treatment and subsequently in 5-minute (Experiment B), 10-minute (Experiment C), and 20-minute (Experiment D) intervals, while the control experiment (Experiment A) introduced 250 mL of the electrochemically generated H_2O_2 solution as one addition at the beginning of the treatment experiment. The additional experimental parameters are given in Section 3.3.1 (vide supra). The treatment efficacies in terms of total COD and TOC removal and treatment efficiencies in terms of COD and TOC removal per mmol H_2O_2 used were examined for each experiment to optimize the H_2O_2 introduction intervals for more efficient use of H_2O_2 and to obtain higher extent of graywater mineralization (**Figure 5**).

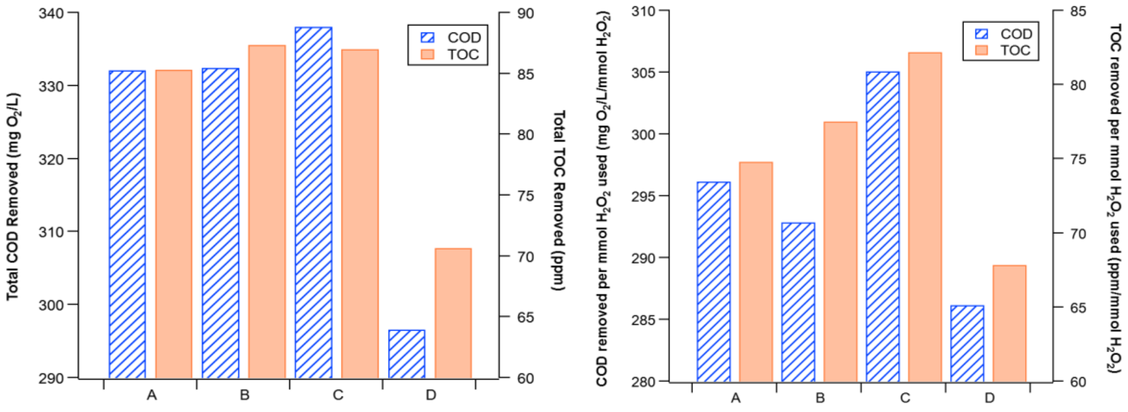

Figure 5. Total COD and TOC removal amounts (a) and COD and TOC removal amounts per mmol H_2O_2 used (b). For the 90-minute treatment timeframe, 250 mL of the H_2O_2 solution were added to the peroxone reactor completely at the beginning in Experiment A, whereas three identical portions of the stage-one reactor solution were applied in the beginning and then at the 5-min and 10-min marks in Experiment B, at the 10-min and 20-min marks in Experiment C, and at the 20-min and 40-min marks in Experiment D.

The loss of treatment efficacy, observed when the entire H_2O_2 solution was introduced simultaneously at the start of treatment is reflective of unreacted H_2O_2 scavenging by ·OH, which accelerated the depletion of H_2O_2 in a non-productive fashion.[29] On the other hand, spacing the H_2O_2 additions during the treatment allowed for the nearly complete reaction of H_2O_2 with O_3 at an optimal stoichiometric mole ratio of 1:2[31] to produce ·OH before the subsequent addition. This approach led to an enhancement in treatment performance. Not only did total COD and TOC removal improve with longer intervals between H_2O_2 injections (**Figure a**), the COD and TOC removal efficiency per mmol H_2O_2 followed the same trend (**Figure b**). However, the longer intervals between each introduction resulted in a lower H_2O_2 concentration than stoichiometrically needed before the following injection. As a result, the peroxone generation was impeded and therefore limited the overall treatment performance. It is important to note that optimal H_2O_2 addition timings may be highly dependent on the composition of wastewater to be treated. For example, wastewater with higher COD (i.e., containing more oxidizable species), may allow for reduced intervals between each H_2O_2 addition and allowing for ·OH to react with the oxidizable substrates. For the synthetic graywater used herein, 10-minute intervals were found to be the optimal condition to achieve the most efficient H_2O_2 use and highest treatment performance.

3.4.5. Electrochemical H_2O_2 Generation with a PTFE-Coated Carbon Paper Cathode

Commercially available carbon-based electrodes (**Table S1**) were characterized and compared in terms of electrocatalytic activity for H_2O_2 production, chemical stability, and cost of material. **Table 2** lists the 60-minute averaged H_2O_2 production rates for each electrode of interest at varying current densities: 1 mA/cm^2, 2 mA/cm^2, and 5 mA/cm^2. For each current density tested, CP75T carbon paper (AVCARB, Lowell, USA) provided the highest H_2O_2 production rate. Moreover, CP75T was coated with PTFE, rendering its surface invulnerable to attacks by weak acids and bases present in wastewater.[32] The PTFE coating not only enhanced chemical stability, but also the mechanical properties of the carbon paper, including tensile strength at break in machine direction, is $F_{TU\ CP75T}$ = 20 MPa for the carbon paper electrode with PTFE coating, compared to $F_{TU\ CP75}$ = 6.5 MPa for the carbon paper electrode without PTFE coating. As a result, CP75T was less susceptible to mechanical stress caused by the bubbling of the O_2 flow in the H_2O_2 chamber than other electrodes without PTFE coating. Lastly, the price of the CP75T was in the middle range among all candidates (0.6875 $/cm^2 on Fuelcellstore.com).

Table 2. 60-minute averaged H_2O_2 production rates for different cathodes as a function of current density. More details about each material can be found in **Table S1** of Supplementary Information.

	1 mA.cm^{-2} (µM/min)	2 mA.cm^{-2} (µM/min)	5 mA.cm^{-2} (µM/min)
CP75T	4.21	14.33	17.97
G100	0.00	0.43	15.40
C100	1.35	5.45	8.91
RVC 80 PPI	2.00	2.42	0.89
MGL 190	0.00	3.85	0.00

The selected PTFE-coated carbon paper was used as a cathode to confirm the H_2O_2 generation via O_2 reduction by performing CV under oxygenated (O_2 purging) and deoxygenated (N_2 purging) conditions. **Figure 6** shows cathodic currents with a reduction peak around –0.4 V vs. Ag/AgCl under O_2 purging, whereas no reduction peak is visible under N_2 purging. Therefore, the reduction of O_2 to H_2O_2 took place at the cathode and appeared as the reduction peak under saturation with O_2.[33] The remaining cathodic currents beyond –0.4 V under the oxygenated and deoxygenated conditions are attributed to hydrogen evolution reaction.

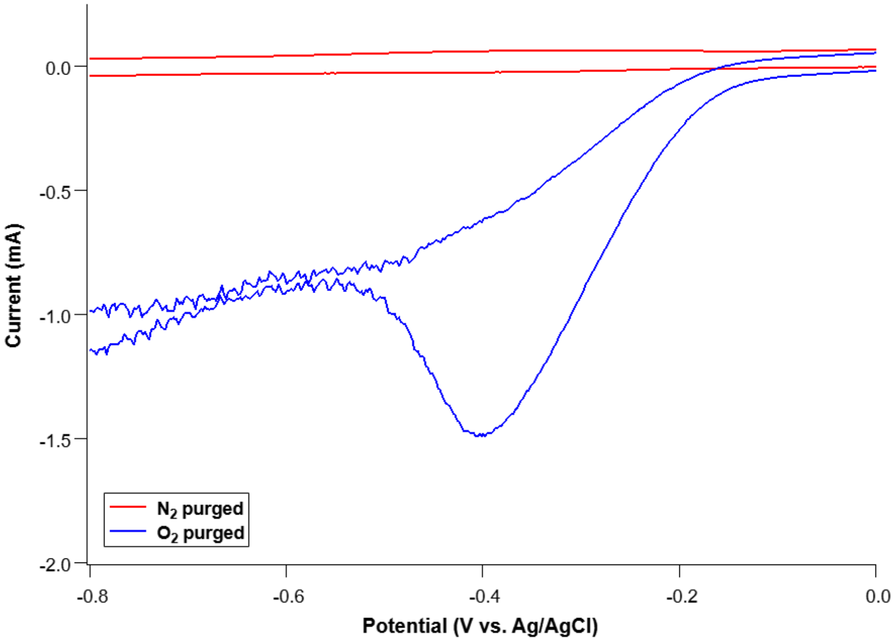

Figure 6. Cyclic voltammograms of PTFE-coated carbon paper electrode under oxygenated and deoxygenated conditions. Characteristic O_2 reduction peak for H_2O_2 production is only visible under saturation with O_2.

3.5. Conclusion

The laboratory-scale treatment of synthetic graywater in an uncoupled E-peroxone process is explored in this study. By separating the in situ electrochemical production of H_2O_2 from the main reaction chamber in which ·OH is generated, the process not only extends the lifetime of the carbon-PTFE electrodes that are susceptible to degradation by ·OH but also allows for a finer control over H_2O_2 utilization to maximize the ·OH formation. Three equal volumes of the electrochemically prepared H_2O_2 solution were added to the main chamber in 10-minute intervals to achieve the highest COD and TOC removals and the most efficient use of H_2O_2. The uncoupled, sequenced E-peroxone process removed 89% of COD, 86% of TOC, 91% of BOD, and 95% lowering of turbidity from synthetic graywater after 90 minutes of treatment. The resulting effluent meets most of the requirements (e.g., COD, TOC, BOD, pH, and turbidity) established in the NSF 350/350-1 standard for the safe discharge and reuse for non-potable water applications such as toilet and urinal flushing. Moreover, the process recycles a portion of the effluent for the subsequent electrochemical production of H_2O_2. The time necessary to reach $[H_2O_2] \approx 4.8$ mM slightly increased from cycle to cycle due to decreasing solution conductivity. Nevertheless, the overall reaction process-maintained removal levels above 85% (COD) and 73% (TOC) over four consecutive cycles without addition of clean water or additional electrolyte solution into the system. The two-stage E-peroxone system can be integrated with other wastewater treatment technologies (e.g., activated carbon or chlorination) to overcome limitations of the E-peroxone process (e.g., nitrogen removal) and to allow for effective onsite treatment of human wastewater in remote areas.

3.6. Supplementary Information

Table S1. Details about carbon-based electrode materials.

Name	Description	Supplier	Thickness (mm)	Bulk density (g/cm^3)
CP75T	Carbon paper with PTFE coating (13%)	AvCarb Material Solutions	0.255	0.33
G100	Soft Graphite Battery Felt	AvCarb Material Solutions	3.2	0.08
C100	Soft Carbon Battery Felt	AvCarb Material Solutions	3.2	0.09
RVC 80 PPI	Duocel Reticulated Vitreous Carbon (RVC) Foam	Duocel Foam	3.175	not provided
MGL 190	Molded Graphite Laminate	AvCarb Material Solutions	0.19	0.44

Table S2. Synthetic graywater recipe adapted from NSF/ANSI 350.

Components	Description	Quantity in 10 L of tap water
Body Wash	Johnson's Gentle Baby Body Moisture Wash	1.59 g
Toothpaste	Colgate® Cavity Protection Toothpaste	0.159 g
Deodorant	Gillette® Clinical Clear Gel Cool Wave	0.106 g
Shampoo	Suave Essentials® Daily Clarifying Shampoo	1.007 g
Conditioner	Suave Essentials® Waterfall Mist Conditioner	1.113 g
Bath Cleaner	Lysol® Disinfectant Bathroom Cleaner	0.53 g
Hand Soap	Dial® Gold Antibacterial Hand Soap	1.219 g
Laundry Detergent	Ultra Tide® Stain Release Laundry Detergent	1.88 mL
Fabric Softener	Ultra Downy® April Fresh Liquid Fabric Softener	0.987 mL
Secondary Effluent	Obtained from the San Jose Creek Water Reclamation Plant	200 mL
L-Lactic Acid	Alfa Aesar, anhydrous, 98%	0.159 g
Na_2SO_4	Macron Fine Chemicals, anhydrous, granular, ACS grade	0.188 g

$NaHCO_3$	Macron Fine Chemicals, ACS grade	0.094 g
Na_3PO_4	Alfa Aesar, tribasic, anhydrous, technical grade	0.188 g

Table S3. Synthetic graywater characteristics and graywater test water parameters defined by the NSF 350/350-1 standard.

Parameter	**Synthetic Graywater**	**NSF 350/350-1 Required Range**
pH	7–8	6.5–8
Temperature (^oC)	20–22	25–35
Chemical oxygen demand (mg O_2/L)	355–362	250–400
Five-day biochemical oxygen demand (mg O_2/L)	155–162	130–180
Total organic carbon (ppm)	83–102	50–100
Total nitrogen (mg N/L)	5.10	3–5*
Total phosphorus (mg P/L)	3.93	1–3
Turbidity (NTU)	11.2$	50–100
E. coli (CFU/100 mL)	$10^{6,\#}$	10^2–10^3
Electrical conductivity (µS/cm)	700	-
Alkalinity (mg $CaCO_3$/L)	142	-

* In total kjeldahl nitrogen.

$ Test dust was not used in synthetic graywater recipe as the system did not have pretreatment steps such as filtration to remove mineral particles in suspension.

The effluent used in synthetic graywater was obtained from the secondary clarifier of the San Jose Creek Water Reclamation Plant instead of the final clarifier as suggested by NSF/ANSI 350.

Figures:

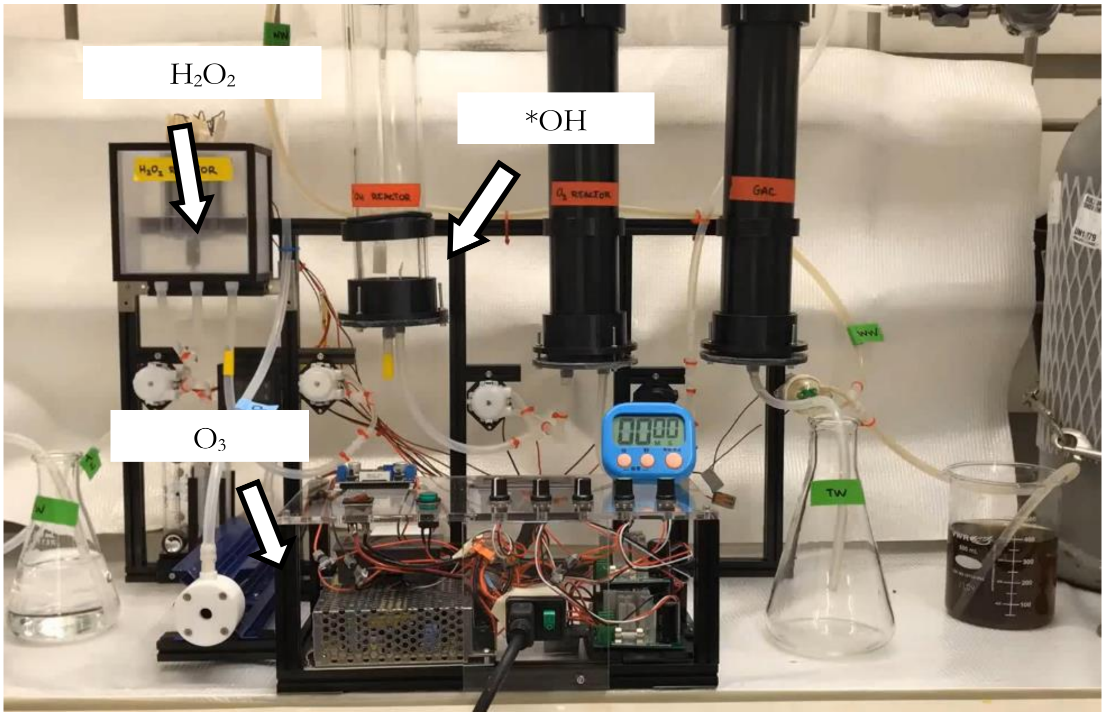

Figure S1. Laboratory-scale prototype.

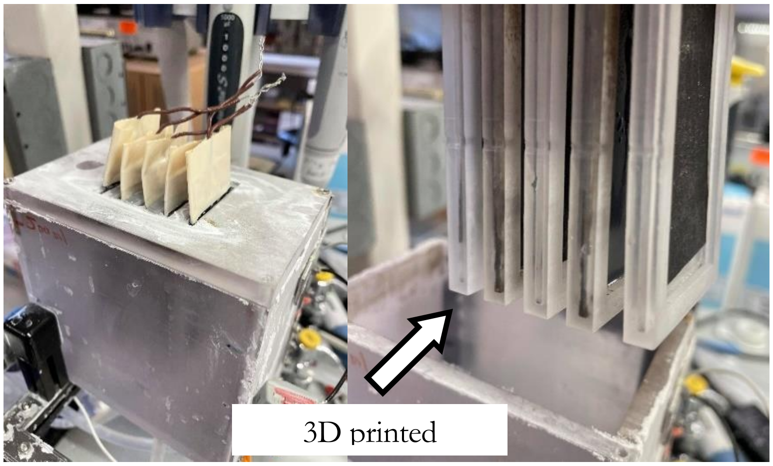

Figure S2. 3D-printed electrodes housing.

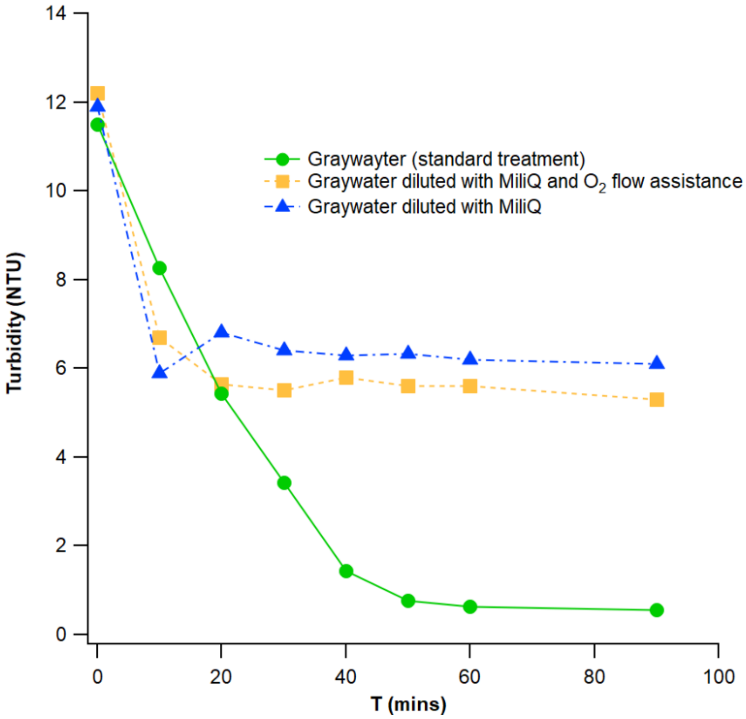

Figure S3. Turbidity trend during single-pass E-peroxone treatment of synthetic graywater. As comparison, synthetic graywater was mixed and diluted with Milli-Q water with and without O_2 sparging. Milli-Q water was added to the graywater at the same dosage as the H_2O_2-containing Na_2SO_4 solution was introduced to the *OH reactor.

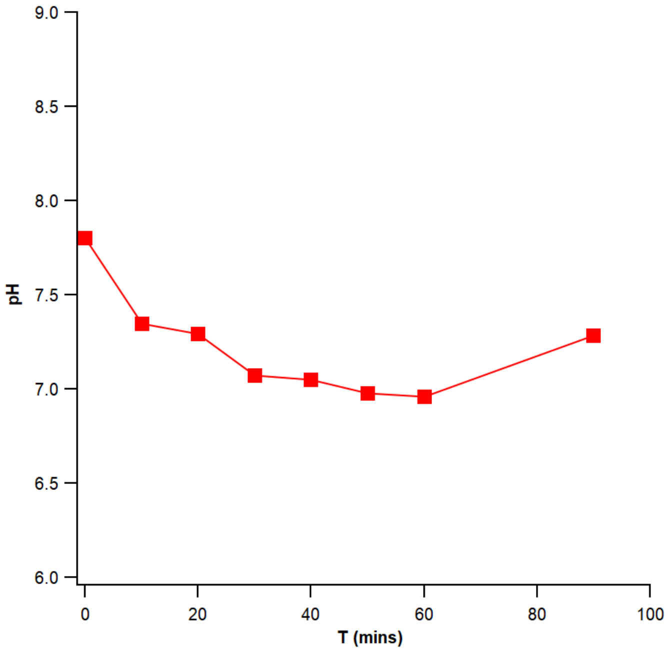

Figure S4. Evolution of pH with time during single-pass E-peroxone treatment of synthetic graywater.

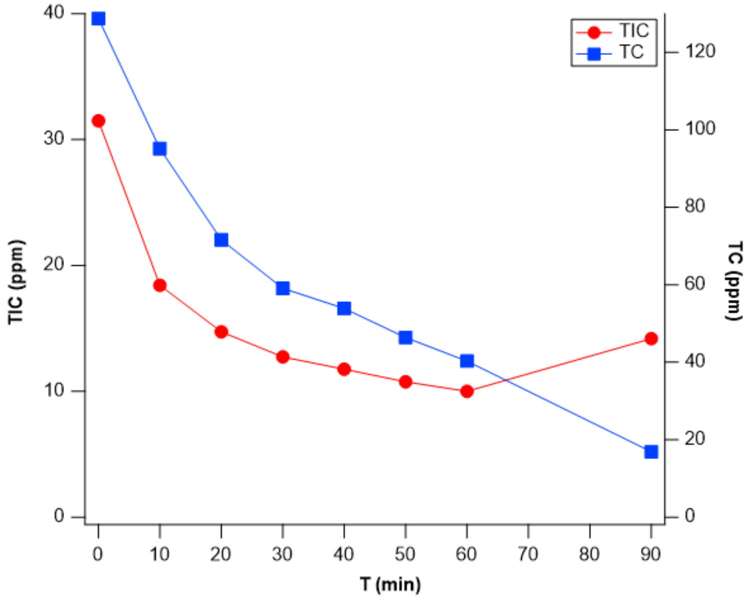

Figure S5. Total inorganic carbon (TIC) and total carbon (TC) trends during single-pass E-peroxone treatment of synthetic graywater. The TIC increased along with the pH from 60-minute to the end of the treatment while TC kept decreasing.

CHAPTER 4: Regeneration of Disinfection-Byproduct-Saturated Activated Carbon Fiber by the Electro-Peroxone Process

4.1. Proposed Research

Coupling the E-peroxone process with activated carbon (AC) fibers for mineralization of disinfection byproducts and regeneration of AC will be investigated. A number of emerging contaminants such as disinfection byproducts have been increasingly detected in the aquatic environment, but conventional wastewater treatments may not be designed to degrade the refractory compounds.[1] Although AC can effectively adsorb and remove the contaminants from wastewater, it cannot degrade them and get regenerated for another adsorption once used. Therefore, the integration of the E-peroxone process and AC will lead to the degradation of disinfection byproducts and furthermore the regeneration of AC as hydroxyl radicals ($\cdot$OH) readily oxidize\ the adsorbed concentrated contaminants from AC. Haloacetic acids (HAA) and trihalomethanes (THM) are chosen as the model disinfection byproducts for this integrated system because they are commonly found in treated wastewater as a result of chlorination. This study will work toward characterizing the adsorption behaviors of HAAs and THMs on AC fibers; evaluating the removal and subsequent mineralization performances of the organic compounds by the E-peroxone process; and, assessing the potential of the E-peroxone process for reuse of the regenerated AC fibers. The final objective of this study is to apply this developed system on a lab-scale pilot reactor and conduct an economic analysis.

The first part of this study will be to investigate the adsorption capacities and kinetics of HAAs and THMs on AC fibers. AC fiber will be characterized for its BET surface area, total pore volume, and pore size distribution by N_2 adsorption isotherms. Then, adsorption isotherms and kinetics of the organic compounds on AC fibers will be studied by implementing isotherm models such as Langmuir and pseudo-first-order/pseudo-second-order models, respectively, for data analysis.[2] The chemical characteristics and interactions of the organic compounds with AC fibers will also be examined to understand their different adsorption capacities and kinetics on AC. As a next step, this study will evaluate the removal efficiencies of HAAs and THMs from AC fibers and the mineralization performance of the compounds and their byproducts by the E-peroxone by measuring their concentrations adsorbed on AC and in the bulk via high-performance liquid chromatography. Additionally, by measuring adsorbed and bulk TOC levels, the mineralization rates of HAAs and THMs will be determined as well as the efficacy of the E-peroxone process for complete mineralization and the chemical composition of the bulk solution throughout the process. For these experiments, AC fiber will be used as cathode to generate H_2O_2 used for ·OH production and to protect its surface from oxidative degradation via cathodic polarization[3], while Ir-Ta-O composite electrode will be used as anode to improve the organic mineralization through mediated oxidation[4].

Lastly, the adsorption capacity and the characteristics of regenerated AC fibers will be analyzed after multiple cycles of adsorption/regeneration to evaluate the viability of the E-peroxone process for reuse of regenerated AC. The evolution of the regeneration efficiency, which quantifies how much THMs and HAAs can be adsorbed on regenerated AC fibers compared to fresh ones, will be tracked after multiple cycles of adsorption followed by E-peroxone regeneration. Furthermore, in order to enhance the regeneration efficiency, the process variables, particularly the dose of ozone, will be optimized. Ozone is known to have potential deteriorative effects on the chemical and textual characteristics of AC surfaces.[3] The optimal dose of ozone will be determined to improve not only the mineralization performance but also the AC regeneration efficiency by the E-peroxone process. With the help of analytical techniques such as scanning electron spectroscopy and Raman spectroscopy, the morphological structure and chemical composition of regenerated AC fibers will be inspected for any potential change after each adsorption/regeneration cycle. The last parts of this study will be to apply this developed technology on a lab-scale pilot reactor where both adsorption and E-peroxone regeneration can occur sequentially, and to perform an economic assessment of the technology (e.g., energy consumption per contaminant removed).

BIBLIOGRAPHY

Chapter 1

(1) Hill, K. Review of The World Health Report 2000: Health Systems: Improving Performance. *Population and Development Review* **2001**, *27* (2), 373–376.

(2) Chirisa, I.; Bandauko, E.; Matamanda, A.; Mandisvika, G. Decentralized Domestic Wastewater Systems in Developing Countries: The Case Study of Harare (Zimbabwe). *Appl Water Sci* **2017**, *7* (3), 1069–1078. https://doi.org/10.1007/s13201-016-0377-4.

(3) Johnson, R. W.; Hultqvist, A.; Bent, S. F. A Brief Review of Atomic Layer Deposition: From Fundamentals to Applications. *Materials Today* **2014**, *17* (5), 236–246. https://doi.org/10.1016/j.mattod.2014.04.026.

(4) Exner, K. S.; Anton, J.; Jacob, T.; Over, H. Controlling Selectivity in the Chlorine Evolution Reaction over RuO2-Based Catalysts. *Angewandte Chemie International Edition* **2014**, *53* (41), 11032–11035. https://doi.org/10.1002/anie.201406112.

(5) Giordano, L.; Cinquini, F.; Pacchioni, G. Tuning the Surface Metal Work Function by Deposition of Ultrathin Oxide Films: Density Functional Calculations. *Phys. Rev. B* **2006**, *73* (4), 045414. https://doi.org/10.1103/PhysRevB.73.045414.

(6) Zazpe, R.; Prikryl, J.; Gärtnerova, V.; Nechvilova, K.; Benes, L.; Strizik, L.; Jäger, A.; Bosund, M.; Sopha, H.; Macak, J. M. Atomic Layer Deposition Al2O3 Coatings Significantly Improve Thermal, Chemical, and Mechanical Stability of Anodic TiO2 Nanotube Layers. *Langmuir* **2017**, *33* (13), 3208–3216. https://doi.org/10.1021/acs.langmuir.7b00187.

(7) Zeng, M.; Peng, X.; Liao, J.; Wang, G.; Li, Y.; Li, J.; Qin, Y.; Wilson, J.; Song, A.; Lin, S. Enhanced Photoelectrochemical Performance of Quantum Dot-Sensitized TiO_2 Nanotube Arrays with Al_2O_3 Overcoating by Atomic Layer Deposition. *Physical Chemistry Chemical Physics* **2016**, *18* (26), 17404–17413. https://doi.org/10.1039/C6CP01299J.

(8) Temperton, R. H.; Gibson, A.; O'Shea, J. N. *In Situ* XPS Analysis of the Atomic Layer Deposition of Aluminium Oxide on Titanium Dioxide. *Physical Chemistry Chemical Physics* **2019**, *21* (3), 1393–1398. https://doi.org/10.1039/C8CP06912C.

(9) Wu, T.; Englehardt, J. D. Peroxone Mineralization of Chemical Oxygen Demand for Direct Potable Water Reuse: Kinetics and Process Control. *Water Research* **2015**, *73*, 362–372. https://doi.org/10.1016/j.watres.2015.01.030.

(10) Wang, Y. The Electro-Peroxone Technology as a Promising Advanced Oxidation Process for Water and Wastewater Treatment. In *Electro-Fenton Process*; Zhou, M., Oturan, M. A., Sirés, I., Eds.; The Handbook of Environmental Chemistry; Springer Singapore: Singapore, 2017; Vol. 61, pp 57–84. https://doi.org/10.1007/698_2017_57.

Chapter 2

(1) Radjenovic, J.; Sedlak, D. L. Challenges and Opportunities for Electrochemical Processes as Next-Generation Technologies for the Treatment of Contaminated Water. *Environ. Sci. Technol.* **2015**, *49* (19), 11292–11302. https://doi.org/10.1021/acs.est.5b02414.

(2) Cho, K.; Hoffmann, M. R. BixTi1–XOz Functionalized Heterojunction Anode with an Enhanced Reactive Chlorine Generation Efficiency in Dilute Aqueous Solutions. *Chem. Mater.* **2015**, *27* (6), 2224–2233. https://doi.org/10.1021/acs.chemmater.5b00376.

(3) A. Martínez-Huitle, C.; Ferro, S. Electrochemical Oxidation of Organic Pollutants for the Wastewater Treatment: Direct and Indirect Processes. *Chemical Society Reviews* **2006**, *35* (12), 1324–1340. https://doi.org/10.1039/B517632H.

(4) Cho, K.; Qu, Y.; Kwon, D.; Zhang, H.; Cid, C. A.; Aryanfar, A.; Hoffmann, M. R. Effects of Anodic Potential and Chloride Ion on Overall Reactivity in Electrochemical Reactors Designed for Solar-Powered Wastewater Treatment. *Environmental Science & Technology* **2014**, *48* (4), 2377–2384. https://doi.org/10.1021/es404137u.

(5) Cho, K.; Kwon, D.; Hoffmann, M. R. Electrochemical Treatment of Human Waste Coupled with Molecular Hydrogen Production. *RSC Adv.* **2013**, *4* (9), 4596–4608. https://doi.org/10.1039/C3RA46699J.

(6) Scherson, Y. D.; Criddle, C. S. Recovery of Freshwater from Wastewater: Upgrading Process Configurations To Maximize Energy Recovery and Minimize Residuals. *Environ. Sci. Technol.* **2014**, *48* (15), 8420–8432. https://doi.org/10.1021/es501701s.

(7) Hoffmann, M. R.; Martin, S. T.; Choi, Wonyong.; Bahnemann, D. W. Environmental Applications of Semiconductor Photocatalysis. *Chemical Reviews* **1995**, *95* (1), 69–96. https://doi.org/10.1021/cr00033a004.

(8) Yang, Y.; Kao, L. C.; Liu, Y.; Sun, K.; Yu, H.; Guo, J.; Liou, S. Y. H.; Hoffmann, M. R. Cobalt-Doped Black TiO2 Nanotube Array as a Stable Anode for Oxygen Evolution and Electrochemical Wastewater Treatment. *ACS Catal.* **2018**, *8* (5), 4278–4287. https://doi.org/10.1021/acscatal.7b04340.

(9) Finke, C. E.; Omelchenko, S. T.; Jasper, J. T.; Lichterman, M. F.; Read, C. G.; Lewis, N. S.; Hoffmann, M. R. Enhancing the Activity of Oxygen-Evolution and Chlorine-Evolution Electrocatalysts by Atomic Layer Deposition of TiO_2. *Energy & Environmental Science* **2019**, *12* (1), 358–365. https://doi.org/10.1039/C8EE02351D.

(10) Naldoni, A.; Allieta, M.; Santangelo, S.; Marelli, M.; Fabbri, F.; Cappelli, S.; Bianchi, C. L.; Psaro, R.; Dal Santo, V. Effect of Nature and Location of Defects on Bandgap Narrowing in Black TiO2 Nanoparticles. *J. Am. Chem. Soc.* **2012**, *134* (18), 7600–7603. https://doi.org/10.1021/ja3012676.

(11) Seok, D.; Wu, M.; Shim, K. B.; Kang, Y.; Jung, H.-K. High-Rate Performance of Ti3$\mathplus$self-Doped TiO2prepared by Imidazole Reduction for Li-Ion Batteries. *Nanotechnology* **2016**, *27* (43), 435401. https://doi.org/10.1088/0957-4484/27/43/435401.

(12) Yang, Y.; Hoffmann, M. R. Synthesis and Stabilization of Blue-Black TiO_2 Nanotube Arrays for Electrochemical Oxidant Generation and Wastewater Treatment.

Environmental Science & Technology **2016**, *50* (21), 11888–11894. https://doi.org/10.1021/acs.est.6b03540.

(13) Exner, K. S.; Anton, J.; Jacob, T.; Over, H. Controlling Selectivity in the Chlorine Evolution Reaction over RuO2-Based Catalysts. *Angewandte Chemie International Edition* **2014**, *53* (41), 11032–11035. https://doi.org/10.1002/anie.201406112.

(14) Kim, W.; Tachikawa, T.; Monllor-Satoca, D.; Kim, H.; Majima, T.; Choi, W. Promoting Water Photooxidation on Transparent WO3 Thin Films Using an Alumina Overlayer. *Energy Environ. Sci.* **2013**, *6* (12), 3732. https://doi.org/10.1039/c3ee42151a.

(15) Sopha, H.; Salian, G. D.; Zazpe, R.; Prikryl, J.; Hromadko, L.; Djenizian, T.; Macak, J. M. ALD Al_2O_3 -Coated TiO_2 Nanotube Layers as Anodes for Lithium-Ion Batteries. *ACS Omega* **2017**, *2* (6), 2749–2756. https://doi.org/10.1021/acsomega.7b00463.

(16) Gui, Q.; Xu, Z.; Zhang, H.; Cheng, C.; Zhu, X.; Yin, M.; Song, Y.; Lu, L.; Chen, X.; Li, D. Enhanced Photoelectrochemical Water Splitting Performance of Anodic TiO2 Nanotube Arrays by Surface Passivation. *ACS Appl. Mater. Interfaces* **2014**, *6* (19), 17053–17058. https://doi.org/10.1021/am504662w.

(17) Bulusu, A.; Kim, H.; Samet, D.; Graham, S. Improving the Stability of Atomic Layer Deposited Alumina Films in Aqueous Environments with Metal Oxide Capping Layers. *J. Phys. D: Appl. Phys.* **2013**, *46* (8), 084014. https://doi.org/10.1088/0022-3727/46/8/084014.

(18) Zazpe, R.; Prikryl, J.; Gärtnerova, V.; Nechvilova, K.; Benes, L.; Strizik, L.; Jäger, A.; Bosund, M.; Sopha, H.; Macak, J. M. Atomic Layer Deposition Al2O3 Coatings Significantly Improve Thermal, Chemical, and Mechanical Stability of Anodic TiO2 Nanotube Layers. *Langmuir* **2017**, *33* (13), 3208–3216. https://doi.org/10.1021/acs.langmuir.7b00187.

(19) Benchmarking Heterogeneous Electrocatalysts for the Oxygen Evolution Reaction | Journal of the American Chemical Society https://pubs.acs.org/doi/abs/10.1021/ja407115p (accessed 2022 -03 -18).

(20) Medford, A. J.; Vojvodic, A.; Hummelshøj, J. S.; Voss, J.; Abild-Pedersen, F.; Studt, F.; Bligaard, T.; Nilsson, A.; Nørskov, J. K. From the Sabatier Principle to a Predictive Theory of Transition-Metal Heterogeneous Catalysis. *Journal of Catalysis* **2015**, *328*, 36–42. https://doi.org/10.1016/j.jcat.2014.12.033.

(21) Kibsgaard, J.; Tsai, C.; Chan, K.; D. Benck, J.; K. Nørskov, J.; Abild-Pedersen, F.; F. Jaramillo, T. Designing an Improved Transition Metal Phosphide Catalyst for Hydrogen Evolution Using Experimental and Theoretical Trends. *Energy & Environmental Science* **2015**, *8* (10), 3022–3029. https://doi.org/10.1039/C5EE02179K.

(22) Kibsgaard, J.; Jaramillo, T. F. Molybdenum Phosphosulfide: An Active, Acid-Stable, Earth-Abundant Catalyst for the Hydrogen Evolution Reaction. *Angewandte Chemie International Edition* **2014**, *53* (52), 14433–14437. https://doi.org/10.1002/anie.201408222.

(23) Koo, M. S.; Cho, K.; Yoon, J.; Choi, W. Photoelectrochemical Degradation of Organic Compounds Coupled with Molecular Hydrogen Generation Using Electrochromic TiO2 Nanotube Arrays. *Environ. Sci. Technol.* **2017**, *51* (11), 6590–6598. https://doi.org/10.1021/acs.est.7b00774.

(24) Pan, X.; Yang, M.-Q.; Fu, X.; Zhang, N.; Xu, Y.-J. Defective TiO 2 with Oxygen Vacancies: Synthesis, Properties and Photocatalytic Applications. *Nanoscale* **2013**, *5* (9), 3601–3614. https://doi.org/10.1039/C3NR00476G.

(25) Ganapathy, V.; Karunagaran, B.; Rhee, S.-W. Improved Performance of Dye-Sensitized Solar Cells with TiO2/Alumina Core–Shell Formation Using Atomic Layer Deposition. *Journal of Power Sources* **2010**, *195* (15), 5138–5143. https://doi.org/10.1016/j.jpowsour.2010.01.085.

(26) Ngo, T. Q.; Goble, N. J.; Posadas, A.; Kormondy, K. J.; Lu, S.; McDaniel, M. D.; Jordan-Sweet, J.; Smith, D. J.; Gao, X. P. A.; Demkov, A. A.; Ekerdt, J. G. Quasi-Two-Dimensional Electron Gas at the Interface of γ-Al2O3/SrTiO3 Heterostructures Grown by Atomic Layer Deposition. *Journal of Applied Physics* **2015**, *118* (11), 115303. https://doi.org/10.1063/1.4930575.

(27) Zhang, Z.; Hedhili, M. N.; Zhu, H.; Wang, P. Electrochemical Reduction Induced Self-Doping of Ti3+ for Efficient Water Splitting Performance on TiO2 Based Photoelectrodes. *Phys. Chem. Chem. Phys.* **2013**, *15* (37), 15637–15644. https://doi.org/10.1039/C3CP52759J.

(28) Kwoka, M.; Galstyan, V.; Comini, E.; Szuber, J. Pure and Highly Nb-Doped Titanium Dioxide Nanotubular Arrays: Characterization of Local Surface Properties. *Nanomaterials* **2017**, *7* (12), 456. https://doi.org/10.3390/nano7120456.

(29) Xiong, L.-B.; Li, J.-L.; Yang, B.; Yu, Y. Ti 3 + in the Surface of Titanium Dioxide: Generation, Properties and Photocatalytic Application. *Journal of Nanomaterials* **2012**, *2012*, 1–13. https://doi.org/10.1155/2012/831524.

(30) Hu, Y. H. A Highly Efficient Photocatalyst—Hydrogenated Black TiO2 for the Photocatalytic Splitting of Water. *Angewandte Chemie International Edition* **2012**, *51* (50), 12410–12412. https://doi.org/10.1002/anie.201206375.

(31) Temperton, R. H.; Gibson, A.; O'Shea, J. N. *In Situ* XPS Analysis of the Atomic Layer Deposition of Aluminium Oxide on Titanium Dioxide. *Physical Chemistry Chemical Physics* **2019**, *21* (3), 1393–1398. https://doi.org/10.1039/C8CP06912C.

(32) Yang, Y.; Zhang, S.; Wang, S.; Zhang, K.; Wang, H.; Huang, J.; Deng, S.; Wang, B.; Wang, Y.; Yu, G. Ball Milling Synthesized MnOx as Highly Active Catalyst for Gaseous POPs Removal: Significance of Mechanochemically Induced Oxygen Vacancies. *Environ. Sci. Technol.* **2015**, *49* (7), 4473–4480. https://doi.org/10.1021/es505232f.

(33) Batra, N.; Gope, J.; Vandana; Panigrahi, J.; Singh, R.; Singh, P. K. Influence of Deposition Temperature of Thermal ALD Deposited Al2O3 Films on Silicon Surface Passivation. *AIP Advances* **2015**, *5* (6), 067113. https://doi.org/10.1063/1.4922267.

(34) Chen, C. L.; Dong, C.-L.; Chen, C.-H.; Wu, J.-W.; Lu, Y.-R.; Lin, C.-J.; Liou, S. Y. H.; Tseng, C.-M.; Kumar, K.; Wei, D.-H.; Guo, J.; Chou, W.-C.; Wu, M.-K. Electronic Properties of Free-Standing TiO2 Nanotube Arrays Fabricated by Electrochemical Anodization. *Phys Chem Chem Phys* **2015**, *17* (34), 22064–22071. https://doi.org/10.1039/c5cp02888d.

(35) Augustsson, A.; Henningsson, A.; Butorin, S. M.; Siegbahn, H.; Nordgren, J.; Guo, J.-H. Lithium Ion Insertion in Nanoporous Anatase TiO2 Studied with RIXS. *J. Chem. Phys.* **2003**, *119* (7), 3983–3987. https://doi.org/10.1063/1.1591735.

(36) Plumb, N. C.; Kobayashi, M.; Salluzzo, M.; Razzoli, E.; Matt, C. E.; Strocov, V. N.; Zhou, K. J.; Shi, M.; Mesot, J.; Schmitt, T.; Patthey, L.; Radović, M. Evolution of the SrTiO3 Surface Electronic State as a Function of LaAlO3 Overlayer Thickness. *Applied Surface Science* **2017**, *412*, 271–278. https://doi.org/10.1016/j.apsusc.2017.03.208.

(37) Seok, T. J.; Liu, Y.; Choi, J. H.; Kim, H. J.; Kim, D. H.; Kim, S. M.; Jang, J. H.; Cho, D.-Y.; Lee, S. W.; Park, T. J. In Situ Observation of Two-Dimensional Electron Gas Creation at the Interface of an Atomic Layer-Deposited Al_2O_3/TiO_2 Thin-Film Heterostructure. *Chem. Mater.* **2020**, *32* (18), 7662–7669. https://doi.org/10.1021/acs.chemmater.0c01572.

(38) Hardin, W. G.; Mefford, J. T.; Slanac, D. A.; Patel, B. B.; Wang, X.; Dai, S.; Zhao, X.; Ruoff, R. S.; Johnston, K. P.; Stevenson, K. J. Tuning the Electrocatalytic Activity of Perovskites through Active Site Variation and Support Interactions. *Chem. Mater.* **2014**, *26* (11), 3368–3376. https://doi.org/10.1021/cm403785q.

(39) Yang, Y.; Shin, J.; Jasper, J. T.; Hoffmann, M. R. Multilayer Heterojunction Anodes for Saline Wastewater Treatment: Design Strategies and Reactive Species Generation Mechanisms. *Environ. Sci. Technol.* **2016**, *50* (16), 8780–8787. https://doi.org/10.1021/acs.est.6b00688.

Chapter 3

(1) Cayan, D. R.; Das, T.; Pierce, D. W.; Barnett, T. P.; Tyree, M.; Gershunov, A. Future dryness in the southwest US and the hydrology of the early 21st century drought. Proc. Natl. Acad. Sci. U. S. A. 2010, 107 (50), 21271−21276.

(2) Sivakumar, B. Global climate change and its impacts on water resources planning and management: assessment and challenges. Stochastic Environmental Research and Risk Assessment 2011, 25 (4), 583−600.

(3) Ghernaout, D. Water Reuse (WR): The Ultimate and Vital Solution for Water Supply Issues. International Journal of Sustainable Development Research 2017, 3 (4), 36.

(4) Sahondo, T.; Hennessy, S.; Sindall, R. C.; Chaudhari, H.; Teleski, S.; Lynch, B. J.; Sellgren, K. L.; Stoner, B. R.; Grego, S.; Hawkins, B. T. Field testing of a household-scale onsite blackwater treatment system in South Africa. Sci. Total Environ. 2020, 703, 135469.

(5) Varigala, S. K.; Hegarty-Craver, M.; Krishnaswamy, S.; Madhavan, P.; Basil, M.; Rosario, P.; Raj, A.; Barani, V.; Cid, C. A.; Grego, S.; Luettgen, M. Field testing of an onsite sanitation system on apartment building blackwater using biological treatment and electrochemical disinfection. Environmental Science: Water Research & Technology 2020, 6 (5), 1400−1411.

(6) Wu, T.; Englehardt, J. D. Peroxone mineralization of chemical oxygen demand for direct potable water reuse: Kinetics and process control. Water Res. 2015, 73, 362−372.

(7) Bruursema, T. The new NSF 350 and 350-1. Plumbing Systems & Design Magazine 2011, 15.

(8) Li, F.; Wichmann, K.; Otterpohl, R. Review of the technological approaches for grey water treatment and reuses. Sci. Total Environ. 2009, 407 (11), 3439−3449.

(9) Reif, R.; Omil, F.; Lema, J. M. Removal of pharmaceuticals by membrane bioreactor (MBR) technology. In Comprehensive Analytical Chemistry; Elsevier: 2013; Vol. 62, pp 287−317.

(10) Weavers, L. K.; Malmstadt, N.; Hoffmann, M. R. Kinetics and mechanism of pentachlorophenol degradation by sonication, ozonation, and sonolytic ozonation. Environ. Sci. Technol. 2000, 34 (7), 1280−1285. (11) Gassie, L. W.; Englehardt, J. D. Advanced oxidation and disinfection processes for onsite net-zero greywater reuse: A review. Water Res. 2017, 125, 384−399.

(12) Wang, Y. The electro-peroxone technology as a promising advanced oxidation process for water and wastewater treatment. In Electro-Fenton Process; Springer, 2017; pp 57−84.

(13) International Organization for Standardization. Non-sewered sanitation systems □ Prefabricated integrated treatment units □ General safety and performance requirements for design and testing; ISO 30500:2018.

(14) Sellers, R. M. Spectrophotometric determination of hydrogen peroxide using potassium titanium(IV) oxalate. Analyst 1980, 105 (1255), 950−954.

(15) Bisutti, I.; Hilke, I.; Raessler, M. Determination of total organic carbon - an overview of current methods. TrAC, Trends Anal. Chem. 2004, 23 (10), 716−726.

(16) Water Environmental Federation; American Public Health Association. Standard Methods for the Examination of Water and Wastewater; American Public Health Association (APHA): Washington, DC, 2005.

(17) Onsite Residential and Commercial Water Reuse Treatment Systems; NSF/ANSI 350, 2011.

(18) Eriksson, E.; Andersen, H. R.; Madsen, T. S.; Ledin, A. Greywater pollution variability and loadings. Ecological engineering 2009, 35 (5), 661−669.

(19) Amor, C.; Marchao, L.; Lucas, M. S.; Peres, J. A. Application of˜ Advanced Oxidation Processes for the Treatment of Recalcitrant Agro-Industrial Wastewater: A Review. Water 2019, 11 (2), 205.

(20) Cohen, Y.; Kirchmann, H. Increasing the pH of wastewater to high levels with different gases□CO 2 stripping. Water, Air, Soil Pollut. 2004, 159 (1), 265−275.

(21) Moghadam, F. N.; Hamidmousavi, R. S.; Dashti, I.; Moghadm, M. N. Evaluating the efficiency of phosphorus removal in aqueous solutions by Fenton method. International Journal of Current Research 2016, 8 (12), 43662−43665.

(22) Kasak, K.; Karabelnik, K.; Kõiv, M.; Jenssen, P.; Mander, Ü. Phosphorus removal from greywater in an experimental hybrid compact filter system. WIT Trans. Ecol. Environ. 2011, 145, 649−657.

(23) Lin, S. H.; Chang, C. C. Treatment of landfill leachate by combined electro-Fenton oxidation and sequencing batch reactor method. Water Res. 2000, 34 (17), 4243−4249.

(24) Asada, T.; Ohkubo, T.; Kawata, K.; Oikawa, K. Ammonia adsorption on bamboo charcoal with acid treatment. J. Health Sci. 2006, 52 (5), 585−589.

(25) Pressley, T. A.; Bishop, D. F.; Roan, S. G. Ammonia-nitrogen removal by breakpoint chlorination. Environ. Sci. Technol. 1972, 6 (7), 622−628.

(26) Cho, K.; Hoffmann, M. R. Urea Degradation by Electrochemically Generated Reactive Chlorine Species: Products and Reaction Pathways. Environ. Sci. Technol. 2014, 48 (19), 11504−11511.

(27) Connick, R. E. The interaction of hydrogen peroxide and hypochlorous acid in acidic solutions containing chloride ion. J. Am. Chem. Soc. 1947, 69 (6), 1509−1514.

(28) Kovács, N.; Grozovski, V.; Moreno-García, P.; Broekmann, P.; Vesztergom, S. A Model for the Faradaic Efficiency of Base Metal Electrodeposition from Mildly Acidic Baths to Rotating Disk Electrodes. J. Electrochem. Soc. 2020, 167 (10), 102510.

(29) Mavrikis, S.; Perry, S. C.; Leung, P. K.; Wang, L.; Ponce de León, C. Recent Advances in Electrochemical Water Oxidation to Produce Hydrogen Peroxide: A Mechanistic Perspective. ACS Sustainable Chem. Eng. 2021, 9, 76−91.

(30) Christensen, H.; Sehested, K.; Corfitzen, H. Reactions of hydroxyl radicals with hydrogen peroxide at ambient and elevated temperatures. J. Phys. Chem. 1982, 86 (9), 1588−1590.

(31) Buxton, G. V.; Greenstock, C. L.; Helman, W. P.; Ross, A. B. Critical review of rate constants for reactions of hydrated electrons, hydrogen atoms and hydroxyl radicals (· OH/· O- in aqueous solution. J. Phys. Chem. Ref. Data 1988, 17 (2), 513−886.

(32) Fischbacher, A.; von Sonntag, J.; von Sonntag, C.; Schmidt, T. C. The• OH radical yield in the H2O2+ O3 (peroxone) reaction. Environ. Sci. Technol. 2013, 47 (17), 9959−9964.

(33) Puts, G. J.; Crouse, P.; Ameduri, B. M. Polytetrafluoroethylene: synthesis and characterization of the original extreme polymer. Chem. Rev. 2019, 119 (3), 1763−1805.

(34) Li, Y.; Zhang, Y.; Xia, G.; Zhan, J.; Yu, G.; Wang, Y. Evaluation of the technoeconomic feasibility of electrochemical hydrogen peroxide production for decentralized water treatment. Front. Environ. Sci. Eng. 2021, 15 (1), 1.

(35) Walter, C.; Kummer, K.; Vyalikh, D.; Brüser, V.; Quade, A.; Weltmann, K.-D. Using a Dual Plasma Process to Produce CobaltPolypyrrole Catalysts for the Oxygen Reduction Reaction in Fuel Cells: I. Characterization of the Catalytic Activity and Surface Structure. J. Electrochem. Soc. 2012, 159 (8), F494.

Chapter 4

(1) Bernal, V.; Erto, A.; Giraldo, L.; Moreno-Piraján, J. C. Effect of Solution PH on the Adsorption of Paracetamol on Chemically Modified Activated Carbons. *Molecules* **2017**, *22* (7), 1032. https://doi.org/10.3390/molecules22071032.

(2) Trellu, C.; Oturan, N.; Keita, F. K.; Fourdrin, C.; Pechaud, Y.; Oturan, M. A. Regeneration of Activated Carbon Fiber by the Electro-Fenton Process. *Environ. Sci. Technol.* **2018**, *52* (13), 7450–7457. https://doi.org/10.1021/acs.est.8b01554.

(3) Bañuelos, J. A.; García-Rodríguez, O.; Rodríguez-Valadez, F. J.; Manríquez, J.; Bustos, E.; Rodríguez, A.; Godínez, L. A. Cathodic Polarization Effect on the Electro-Fenton Regeneration of Activated Carbon. *J Appl Electrochem* **2015**, *45* (5), 523–531. https://doi.org/10.1007/s10800-015-0815-2.

(4) Panizza, M.; Cerisola, G. Direct And Mediated Anodic Oxidation of Organic Pollutants. *Chem. Rev.* **2009**, *109* (12), 6541–6569. https://doi.org/10.1021/cr9001319.